Ice accretion compositions in ice crystal icing

Yasir A Malik, Kilian Köbschall, Stephan Bansmer, Cameron Tropea, Jeanette Hussong, Philippe Villedieu

▶ To cite this version:

> Yasir A Malik, Kilian Köbschall, Stephan Bansmer, Cameron Tropea, Jeanette Hussong, et al.. Ice accretion compositions in ice crystal icing. International Journal of Heat and Mass Transfer, 2023, 220, pp.124910. ⟨10.1016/j.ijheatmasstransfer.2023.124910⟩. ⟨hal-04612192⟩

HAL Id: hal-04612192

https://hal.science/hal-04612192v1

Submitted on 14 Jun 2024

International Journal of Heat and Mass Transfer 220 (2024) 124910

Contents lists available at ScienceDirect

International Journal of Heat and Mass Transfer

journal homepage: www.elsevier.com/locate/ijhmt

Ice accretion compositions in ice crystal icing

Yasir A. Malik [a,*,1], Kilian Köbschall [b,**,1], Stephan Bansmer [c], Cameron Tropea [b], Jeanette Hussong [b], Philippe Villedieu [d]

[a] Technische Universität Braunschweig, Institute of Fluid Mechanics, Hermann Blenk Straße 37, Braunschweig, 38108, Germany
[b] Technische Universität Darmstadt, Institute of Fluid Mechanics and Aerodynamics, Peter-Grünberg-Straße 10, Darmstadt, 64287, Germany
[c] Politechnico Di Milano, Dipartimento di Science e Tecnologie Aerospaziali, Via La Masa 34, Milan, 20156, Italy
[d] ONERA / DMPE, Université de Toulouse, 2 Av. Edouard Belin, Toulouse, 31000, France

ABSTRACT

Ice crystal icing is a major hazard in aviation from the perspectives of aerodynamic deterioration, flight safety and operability. To counter this challenge, existing ice prediction tools require more accurate modeling of sticking efficiency of glaciated ice crystals on heated substrates. As part of the present study, icing wind tunnel experiments have been performed to quantify the volumetric liquid water fraction in the ice layers, the sticking efficiency of impacting ice crystals and the maximum thickness of ice layers accreted on a dedicated test article for a wide range of experimental conditions. To achieve this objective, two measurement techniques, calorimetry and capacitive measurements, have been employed to quantify the average liquid water content and the distribution of liquid in the ice layers. The experiments show that when switching from negative to positive wet bulb temperatures, the sticking efficiency and maximum thickness of ice layers increase significantly. A similar trend is observed for increasing substrate heat flux, which results in an increasing liquid fraction in the ice layer measured by calorimetry, as well as increasing sticking efficiency and maximum thickness of the ice layers. Increasing the ice water content does not have a significant influence on the liquid content, but leads to more pronounced erosion effects. The conducted experiments provide an unprecedented insight into the liquid distribution in ice accretions and its effect on the sticking efficiency. These results provide a sound basis for more accurate modeling of sticking efficiency and enhances the understanding of ice accretion processes.

1. Introduction

Ice crystal icing is considered a major risk in the aviation industry, as it results in detrimental effects on aircraft performance and safety. Ice crystals ingested into the warm environment of a jet engine can fully or partially melt due to local air temperatures above freezing or due to contact with heated surfaces. The generated meltwater facilitates ice accretion, which deteriorates engine performance by causing stall and surge of the compressor. Furthermore, shedding of the accreted ice can extinguish the combustion or cause severe damage to downstream engine components [1]. Thus, the effects of ice crystal icing contribute to reduced economic viability and most significantly to degraded flight safety.

To mitigate these risks, numerical tools for the prediction of ice accretion are required. However, the associated physical phenomena are complex and not yet fully understood. Therefore, a deeper understanding of the underlying mechanisms and the different influences is necessary to enhance numerical models. Moreover, comprehensive experimental data sets are essential to calibrate and validate the numerical tools. The present research focuses on one of the key parameters in the modeling of ice crystal icing, which is the sticking efficiency. The sticking efficiency is defined as the mass fraction of the impacting ice crystals that adheres to a surface [2]. This parameter is crucial in modeling ice accretion, as it instrumentally determines the accreted mass. For mixed-phase clouds, the sticking efficiency has been found to be a function of the melt ratio, i.e., the ratio of liquid water content to total water content in the ice cloud [2]. This relation has been implemented in numerical tools, which have been demonstrated to successfully predict ice accretion [3,4]. However, literature on ice crystal icing caused by fully frozen particles impacting onto heated substrates is sparse. Furthermore, it is expected that the sticking efficiency is a function of the liquid volume fraction present at the impact location [3]. While Currie and Fuleki [5] quantified the liquid fraction in ice accretions on adiabatic test articles, direct measurements of the liquid fraction on heated substrates have not yet been performed due to a lack of wind tunnel instrumentation. The present study aims at providing insights into these

---

* Corresponding author.
** Corresponding author.
E-mail address: y.malik@tu-braunschweig.de (Y.A. Malik).
[1] Contributed equally as co-first authors.

https://doi.org/10.1016/j.ijheatmasstransfer.2023.124910
Received 23 August 2023; Received in revised form 11 October 2023; Accepted 1 November 2023

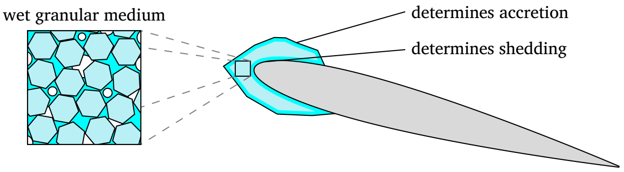

Fig. 1. Schematic composition of an ice accretion and liquid water fraction as the driving force for accretion and shedding.

aspects. The distribution of liquid water in an ice accretion grown on a heated substrate and the major effects determined by its distribution are qualitatively illustrated in Figure 1.

The presence of liquid water is considered as a necessary condition for significant ice accretion and the severity of ice layer growth is determined by the imbibition of water into the porous medium by capillary forces. Kintea et al. [6] successfully modeled shedding of ice accumulations by defining a threshold for the melted fraction at the interface between the substrate and the ice layer. Furthermore, it can be expected that not only adhesive strength but also cohesive strength is strongly affected by the liquid fraction [7]. This is not only relevant for the prediction of shedding, but also for a more in-depth modeling of erosion of the ice accretion phenomena, since the erosion rate depends on the accretion mechanical properties which in turn depend on the liquid fraction. The combined effects of sticking efficiency and the erosion rate determine the accretion process. A better understanding of the liquid fraction of an ice layer and the associated effects serve as the main motivation for this work.

To investigate these effects, experiments are conducted in the TU Braunschweig icing wind tunnel and the accreted ice layers are characterized with respect to thickness and liquid fraction. Two measurement techniques, calorimetry and capacitive sensing, are used to quantify the liquid content. A parametric study is performed to investigate the influence of wet bulb temperature, substrate heat flux and ice water content on liquid volume fraction and sticking efficiency.

2. Experimental facility

An overview of the Braunschweig icing wind tunnel is first presented. Next, the ice crystal generation and conveyance system are described with details about ice crystal size and morphology.

2.1. TU Braunschweig icing wind tunnel

The experiments performed in the framework of this study are conducted in the icing wind tunnel of TU Braunschweig, which is capable of simulating ice crystal icing conditions. A schematic of the wind tunnel is illustrated in Figure 2a. The ice crystals are produced in a cold chamber and injected into the wind tunnel through a pipe. Two separate refrigeration systems cool the wind tunnel and the cold chamber.

The icing wind tunnel has a test section with cross-section $0.5\,\mathrm{m} \times 0.5\,\mathrm{m}$. The flow velocity in the test section can reach up to $40\,\mathrm{m\,s^{-1}}$ and allows for static air temperature down to $-25\,^{\circ}\mathrm{C}$. The relative humidity is not controlled explicitly, but the air in the wind tunnel is generally saturated with water vapor. The wind tunnel does not allow to simulate altitude. The Braunschweig icing wind tunnel is a sea-level facility and the wind tunnel operates at the ambient pressures present in the laboratory, which is at an altitude of 75 m, with ambient pressure of approximately 990 mbar. Further information on the design and capabilities of the wind tunnel can be found in the work of Bansmer et al. [8].

2.2. Ice crystal generation and conveyance system

One of the unique aspects of the TU Braunschweig icing wind tunnel is its ice crystal generation system. Cloud chamber technology is employed to simulate the natural occurring ice crystal generation process as observed in atmospheric clouds. This approach involves feeding atomized water droplets through an air stream into a chamber, in which the conveying air stream is mixed with another cooled air stream. This leads to the growth of naturally shaped ice particles [9,10]. Once the ice crystals reach a critical size they settle down in a chest freezer, which is cooled down to $-60\,^{\circ}\mathrm{C}$. Moreover, the temperature of the cooling chamber where the ice crystal generation and conveyance system is setup is maintained at $-15\,^{\circ}\mathrm{C}$ to allow for transport of fully glaciated ice crystals to the wind tunnel. The cloud chamber-based freeze-out technique for ice crystal production system is depicted in Figure 2b.

The generated ice crystals are moved to a storage freezer, which is also located in the cooling chamber. Just before an experimental run, the newly produced ice crystals are mixed with the stored crystals, which allows to maintain a uniform quality. Larger agglomerates resulting from sintering of crystals are broken up by crushing the prepared ice. The fine ice crystals are then shoveled to a dosing machine from where they are transported to the sieving machine, which is composed of a single sieve with mesh size of 1 mm and conveyed through to the icing wind tunnel test section. The sieving machine is driven by an electric motor that drives a $800\,\mathrm{mm} \times 800\,\mathrm{mm}$ sieve, oscillating at a constant frequency of 8 Hz [8]. The pipes carrying the ice crystals ingest air from the wind tunnel and are additionally cooled. The frequency of the dosing machine determines the target ice water content. Remaining ice crystals that are left on top of the sieving machine at the end of the experimental run are accounted for in calculating the true ice water content.

2.3. Ice crystal size distribution and morphology

Ice crystal icing conditions are normally associated with convective clouds of high ice water content at flight altitude. Images of natural ice crystals taken during previous flight campaigns are shown in Figure 3a and b [8]. Since particle growth is effected by vapor deposition and aggregation and encounters different temperature regimes, a variety of irregular shapes are possible at different altitudes in convective cloud systems.

Exemplary images of ice crystals as they are observed by 2D-S and C-HSI probes in the test section of the icing wind tunnel are depicted in Figure 3c and d. It can be observed that most of the particles feature an irregular, elongated shape [8]. The characteristic size distribution of the generated ice particles is shown in Figure 4. In the Braunschweig icing wind tunnel, the ice particle size distribution is characterized by an MMD of about 80 μm which lies in the range of what is found in the atmosphere and ice particles inside a jet engine. The high number of small ice particles below 80 μm corresponds to particle size distributions in young and aged contrails [11].

To investigate the spatial ice water content uniformity inside the test section a custom-made particle collection tube system was designed. It allowed to measure the relative distribution of ice particle concentration inside the test section. The results reflected acceptable uniformity of ±20 % from the center-line according to ARP 5905 standards over a circular area of about 150 mm in diameter, within which the test article is placed. Further details on IWC spatial uniformity in the BIWT test section have been previously documented in Bansmer et al. [8].

Isokinetic probe (IKP) measurements were carried out for determining the ice particle concentrations inside the BIWT test section and it was ensured that the dosing machine offered a linear operational behavior for different ice water content. During calibration of the ice crystal icing cloud, it was observed that the percentage residuum of ice on the sieving machine was constant for various feed rates. The temporal evolution of the IWC showed that after the first 30 seconds of turning on the icing cloud, the ice crystal icing cloud stabilized in the test section throughout the duration of the experimental runs. Further details on ice crystal icing cloud calibration have been previously documented by Bansmer et al. [8] and Baumert et al. [12].

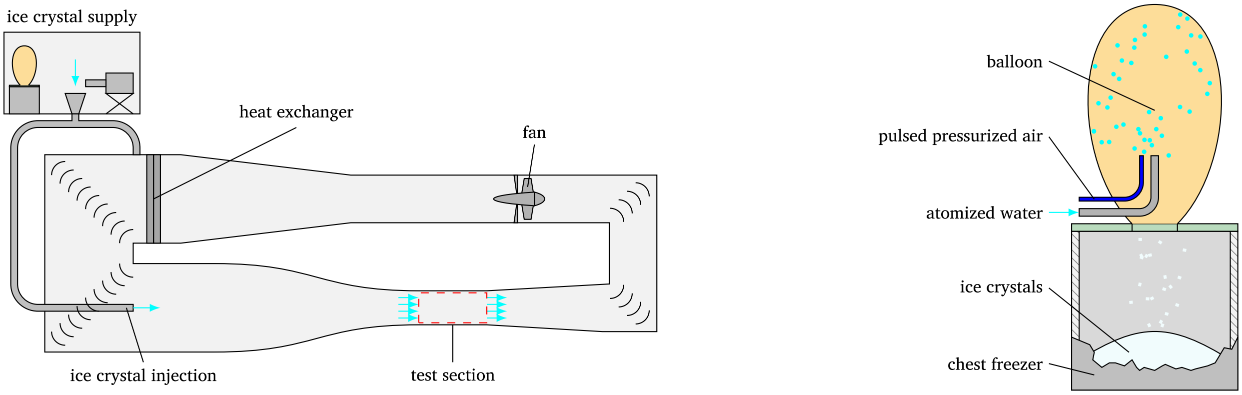

(a) Icing wind tunnel

(b) Cloud chamber

Fig. 2. Schematic illustrations of the TU Braunschweig icing wind tunnel and the cloud chamber for the production of ice crystals.

(a) Convective cloud region, 80 µm median mass diameter, 3 $\mathrm{g\,m^{-3}}$ ice water content and −10 °C air temperature

(b) Stratiform cloud region, 150 µm median mass diameter, 1.2 $\mathrm{g\,m^{-3}}$ ice water content and −10 °C air temperature

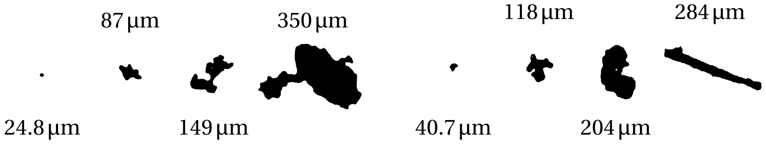

(c) High speed imaging of particles in the wind tunnel at 0 °C and −5 °C and their mass diameters

(d) Particles in the wind tunnel, 79 µm median mass diameter, 3.2 $\mathrm{g\,m^{-3}}$ ice water content and −15 °C air temperature

Fig. 3. Natural ice crystals in different cloud regions recorded during the Darwin Campaign, (a) and (b), and ice crystals in the Braunschweig icing wind tunnel, (c) and (d), for comparison. Adapted from [8], published under CC BY 4.0.

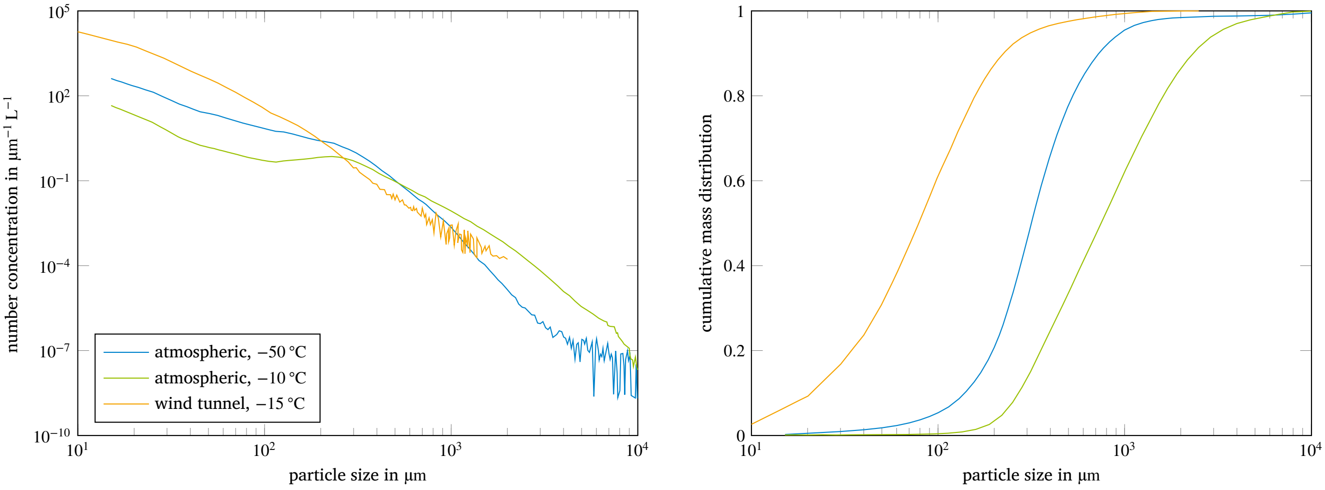

(a) Particle size distribution

(b) Cumulative size distribution

Fig. 4. Particle size distribution of the ice crystal cloud in the Braunschweig icing wind tunnel for an MMD of around 80 µm [8].

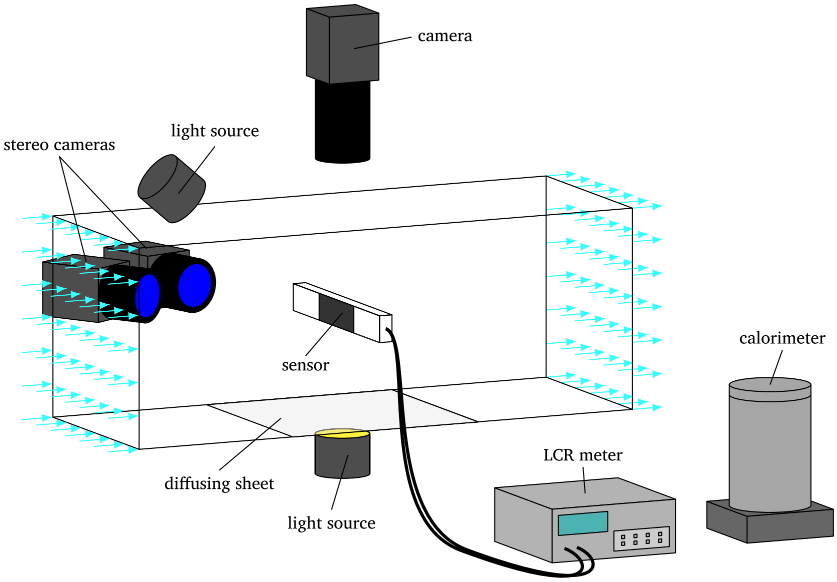

Fig. 5. Measurement equipment and setup in the icing wind tunnel.

2.4. Experimental setup

The setup of the measurement equipment is illustrated in Figure 5. The ice accretion is characterized in terms of thickness and shape by shadowgraphy and stereoscopy. A camera (Canon 80D) located above and a light source below the test article provide shadowgraphy to measure the ice layer thickness. In addition, two cameras (Canon 80D) observing the process from an oblique perspective with an angle of approximately 20° between their lines of sight enable stereoscopy to characterize the shape of the ice accretion (see subsection 3.3). To highlight the structure in the ice layer, facilitating the evaluation of stereoscopy data, another light source is place at an oblique angle and illuminates the ice accretion.

The developed sensor is connected to an LCR meter (Rohde & Schwarz HM8118), which enables recording of the measured capacitance over the course of the experimental run. This input is then utilized to determine the liquid volume water fraction in the ice layer (see subsection 3.2). After each experimental run, the ice layer is removed from the test article by means of an ice scraper and placed inside the calorimeter, which is used to determine the mass fractions of ice and liquid water of the final ice layer. Furthermore, the remaining liquid water left on top of the test article was accounted for by using a dry tissue paper to wipe off the liquid water and measuring the mass of the wet tissue paper. Sufficient measures were taken to enhance the accuracy and limit uncertainties as much as possible. For more details see subsection 3.1. A photograph of the fully assembled test article placed in the test section of the wind tunnel is shown in Figure 6.

For experiments that are conducted at positive wet bulb temperature i.e., wind tunnel temperature warmer than 0 °C, the ice crystals naturally melt due to the warm airflow on their path to the test section and prior to the impact on the test article. The melt ratio of the ice crystals is computed theoretically by applying the model for non-spherical particles proposed by Hauk et al. [13]. For these calculations, the equation of motion of the ice crystals is solved by accounting for their drag in the airflow. The relative velocity and residence time of the ice crystals are calculated for different experimental conditions. These data serve as input to the ice particle melting model.

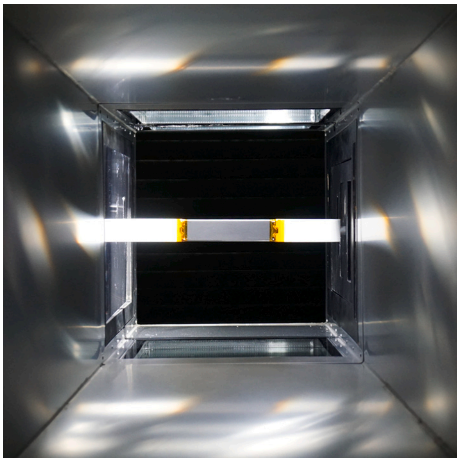

Fig. 6. Flat plate with embedded sensor in the test section of the icing wind tunnel.

Table 1
Overview of experimental conditions to study aerothermal and icing envelope in ICI conditions.

Airspeed in $\mathrm{m\,s^{-1}}$	T_{wb} in °C	IWC in $\mathrm{g\,m^{-3}}$	Heat flux in $\mathrm{kW\,m^{-2}}$
40	-15 to +2.5	4 to 12	4.5 to 12.8

At a wet bulb temperature (T_{wb}) of +2.5 °C and a flow velocity of 40 m s^{-1}, which correspond to the investigated positive wet bulb temperature case in this study, the melt ratio is computed as 32 % based on theoretical modeling research from Hauk et al. [13] and Kintea et al. [6]. Similarly, calculations were carried out for other wet bulb temperatures, as well such as for +1 °C, which resulted in a melt ratio of about 15 %. It was found that the warmer wet bulb temperatures lead to more melting of the ice crystals, enhancing the wetted area and thereby allowing increased sticking contributing to ice accretion growth. Earlier work by Baumert et al. [9] showed that sticking efficiency is approximately proportional to melt ratio of impinging ice crystals, which is relevant for the same icing wind tunnel facility and icing conditions.

Table 1 provides an overview of experimental conditions used to investigate ice crystal icing phenomenon.

3. Measurement techniques

In this section, the different measurement techniques are presented. First, the methods for obtaining the liquid fraction are presented. These comprise calorimetry and capacitive sensing. Second, stereoscopy is outlined, which enables to characterize the ice accretion shape.

3.1. Calorimetry

A mixing calorimeter, as described by Currie and Fuleki [5], is used to measure the liquid mass fraction of the ice accretion. Based on the volume of the accretion measured from stereoscopy, the measured mass fraction is converted to a volume fraction. To minimize heat exchange with the environment during calorimetry, a flat-bottomed dewar flask (FB18 CAL from KGW Isotherm) with a lid on the top is used. To achieve an even temperature distribution in the dewar, a digital magnetic stirrer (RCT 5 from IKA) is used. The initial temperature $T_{cal,1}$ before adding the ice layer and the final temperature T_2 after the ice completely melted and the liquid inside the dewar reached thermal equilibrium are measured with a PT1000 temperature sensor placed inside the dewar. The calorimeter setup is depicted in Figure 7. Prior to the experiment, water acting as the calorimeter liquid is weighed with a precision balance with an accuracy of 10 mg and added to the dewar. After the ice completely melts, the water in the dewar is weighed again to determine the mass of the ice accretion added. The duration for which the ice accretion is exposed to the warm ambient air is kept to a minimum in order to minimize inadvertent melting.

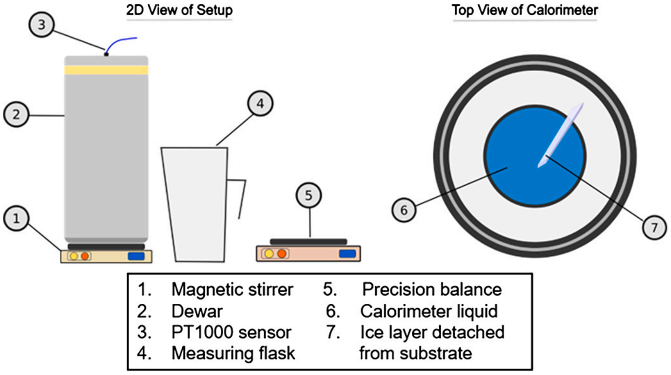

Fig. 7. Calorimetry setup including dewar, magnetic stirrer, measuring flask and precision balance.

The working principle of calorimetry is based on a heat and mass balance before and after adding and melting the sample. The heat balance can be written as [5]

$$m_{ice}\left(c_{p,ice}T_{ice,1}-L_f\right)+m_{liq}c_{p,liq}T_{liq,1}+m_{cal,eff}c_{p,cal}T_{cal,1}=\left[(m_{ice}+m_{liq})c_{p,liq}+m_{cal,eff}c_{p,cal}\right]T_2, \quad (1)$$

where the specific heat capacity of the thawing agent, solid ice and liquid water are denoted by $c_{p,cal}$, $c_{p,ice}$ and $c_{p,liq}$, respectively. The temperature of the ice $T_{ice,1}$ and the liquid water $T_{liq,1}$ in the ice accretion are assumed as 0 °C and the latent heat of fusion is written as L_f. $T_{cal,1}$ is the recorded temperature of the calorimeter liquid prior to the experiment and T_2 is recorded once the calorimeter liquid and the sample reach thermal equilibrium. The effective mass of thawing agent and the mass of ice and liquid water in the ice layer are denoted by $m_{cal,eff}$, m_{ice} and m_{liq}, respectively.

The dewar also has a heat capacity, which results in a change in temperature of the dewar during the process. This heat capacity can be expressed as an additional thawing agent mass by defining a calorimeter constant [5,14]

$$k=m_{cal,eff}-m_{cal} \quad (2)$$

To determine the calorimeter constant k, calibration experiments are performed with liquids of known mass and temperature. The heat balance can then be written as

$$m_{liq}c_{p,liq}T_{liq,1}+\left(m_{cal}+k\right)c_{p,cal}T_{cal,1}=\left[m_{liq}c_{p,liq}+(m_{cal}+k)c_{cal}\right]T_2, \quad (3)$$

with the calorimeter liquid mass and initial temperature m_{cal} and $T_{cal,1}$, the mass and initial temperature of the added liquid m_{liq} and $T_{liq,1}$ and the calorimeter liquid specific heat capacity $c_{p,cal}$, which is evaluated for water at a temperature of $(T_{liq,1}+T_2)/2$.

This heat balance can then be solved for the calorimeter constant k. The measured mass of the calorimeter is roughly 260 g. Over a sample size of 14 measurements the calorimeter constant is evaluated as 28.68 g with an uncertainty of approximately 9 %.

Weighing the final mass of liquid in the calorimeter yields the mass of the ice accretion, i.e., $m_{ice}+m_{liq}$. With Equation (1) the mass of liquid water and ice in the accretion can then be calculated.

The mass fraction of liquid water in the ice layer is then expressed as

$$\frac{LWC}{TWC}=\frac{m_{liq}}{m_{ice}+m_{liq}}. \quad (4)$$

Since numerical simulations make use of the liquid volume fraction, it is beneficial to convert the mass fraction to a volume fraction with

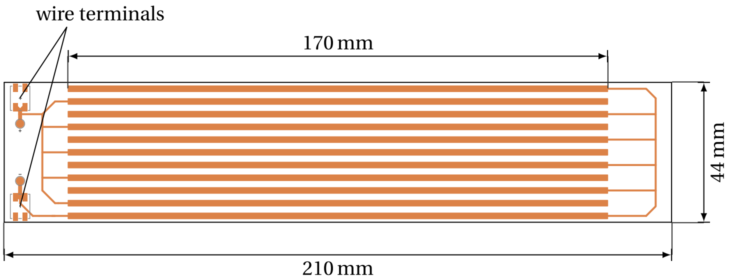

(a) Large-scale sensor with electrode widths and gap widths of 2 mm

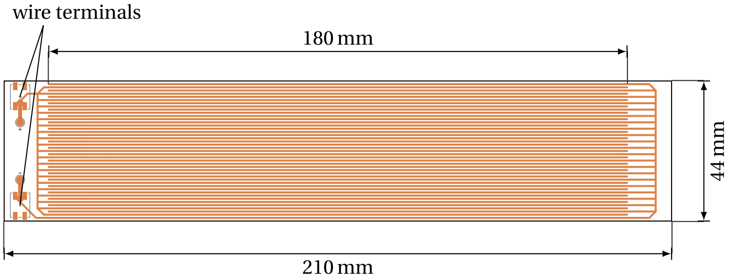

(b) Near-wall sensor with electrode widths and gap widths of 0.5 mm

Fig. 8. Schematics of the two sensors with the wire terminals for connecting the LCR meter on the left and the copper traces acting as electrodes in the center.

$$v_{\mathrm{liq}} = \frac{m_{\mathrm{liq}}}{V_{\mathrm{acc}}\rho_{\mathrm{liq}}}, \tag{5}$$

with the density of liquid water ρ_{liq} and the accreted volume of the ice layer V_{acc} evaluated from stereoscopy.

Furthermore, the mean porosity ϕ and saturation S of the ice layer defined as

$$\phi = 1 - \frac{m_{\mathrm{ice}}}{\rho_{\mathrm{ice}}V_{\mathrm{acc}}} \tag{6}$$

and

$$S = \frac{m_{\mathrm{liq}}}{\phi\rho_{\mathrm{liq}}V_{\mathrm{acc}}} \tag{7}$$

can be calculated. Here ρ_{ice} denotes the density of ice.

3.2. Capacitive sensing

Capacitive sensing of liquid water in the ice accretion is based on the different relative permittivities of the components of the accretion: ice, liquid water and air. The effective relative permittivity of the medium is evaluated from the measured capacitance of the sensor and converted to a liquid fraction.

It is anticipated that the distribution of liquid water in an ice accretion growing at negative wet bulb temperatures is not uniform over the thickness of the accreted layer. Therefore, a single measured capacitance is not sufficient to characterize the water distribution in the accretion. Liquid water is supplied to the ice accretion by melting at the wall. Subsequently, the liquid water is imbibed by the ice accretion due to capillary forces. The ice accretion is cooled by the cold airflow, which can lead to refreezing at the outer surface of the accretion. Furthermore, additional ice crystals that stick to the outer surface bind liquid water. These phenomena lead to a decrease in liquid volume fraction with an increasing distance to the heated wall.

In order to capture the non-uniformity of the water distribution, two capacitive sensors are designed: One sensor that measures the liquid fraction close to the heated wall and another sensor that measures the liquid fraction on a larger scale. The penetration depth of the electric field is determined by the geometry of the electrodes.

In the following, first the design of the sensors and the test article are described. Second, the conversion from the measured capacitance to a liquid volume fraction and its distribution in the ice accretion are outlined.

3.2.1. Sensor and test article design

The capacitive sensors designed for this study are realized as interdigitated electrodes on a solid substrate. The dimensions of the two sensors employed for this study are given in Figure 8. The geometry, which is mainly defined by the width of the electrodes and the width of the gaps between the electrodes, has been determined with the aid of numerical simulations of the electric field. Based on these simulations, one sensor is designed with electrode widths and gap widths of 2 mm each. For the second sensor, the electrode and gap widths are chosen as 0.5 mm. Due to the extended range of sensitivity of the first sensor in comparison to the second sensor, the first sensor is referred to as the large-scale sensor, while the second sensor is referred to as the near-wall sensor.

The sensitivity of both sensors decreases with increasing distance from the substrate. For the large-scale sensor, material further than 5 mm away from the sensor contributes to the measured capacitance by only about 1 %. Analogously, material beyond 1 mm away from the near-wall sensor surface only contributes to the capacitance by 1 %. The near-wall sensor focuses on the region close to the substrate. While the large-scale sensor also covers this region, it includes the liquid fraction beyond a distance of 1 mm from the substrate. Details on the estimation of the distribution of liquid volume fraction in the ice accretion follow in subsubsection 3.2.2.

The two sensors have to be spatially separated to prevent interference. Thus, they are realized on two separate substrates. However, due to an expected nonuniformity of the ice layer, the two sensors cannot measure at the same time, since one of them could collect more ice than the other. Furthermore, this would require two LCR meters for reading the capacitances. Instead, the experiment is first conducted with one sensor, which is subsequently exchanged for the other sensor and the experiment is repeated. The validity of this method relies on the repeatability of the experiments, which was assessed as sufficient for this approach.

The composition of the test article is shown in Figure 9. The capacitive sensors are applied as 18 μm thick copper traces on the substrate. The copper layer is protected by a black solder mask, i.e., a lacquer-like polymer coating. The substrate is made of aluminum nitride. This ceramic acts as an electrical insulator but at the same time exhibits a high

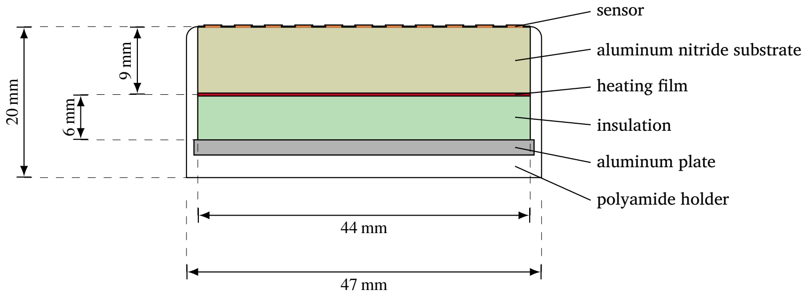

Fig. 9. Structure of the flat plate setup.

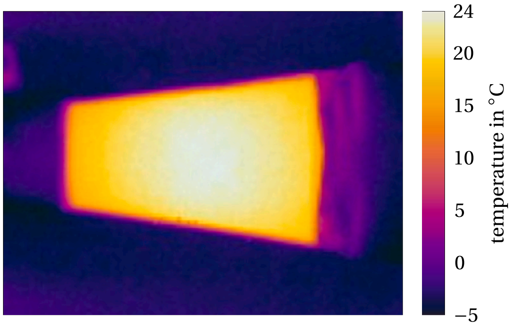

Fig. 10. Uniformity of surface temperature measured with an infrared camera. The plate is captured at an oblique angle from outside of the wind tunnel.

thermal conductivity of approximately 200 W m^{-1} K^{-1}. The high thermal conductivity allows an increased distance to the heater, which is placed at the back of the aluminum nitride plate. The plate has a thickness of 9 mm and thus reduces disturbances, which the electric heating film could cause for the capacitive measurement. The heating film covers the entire back of the plate in order to provide a uniform heat flux.

Thermal insulation with a thickness of 6 mm and a thermal conductivity of 0.2 W m^{-1} K^{-1} is mounted behind the heating film. Then comes an aluminum plate of 2 mm thickness to increase the rigidity of the structure. Finally, the entire stack is enclosed from the back and the sides by a polyamide holder. The polyamide structure is 3 mm thick at the back and 1.5 mm thick at the sides. The thermal conductivity of polyamide is approximately 0.25 W m^{-1} K^{-1}. The thermal resistances between the heater and the different surfaces of the test article suggest that the side walls and the back can be approximated as being adiabatic. Therefore, heat transfer is considered to occur approximately one-dimensional through the aluminum nitride substrate.

Figure 10 shows the surface temperature of the test article captured with an infrared camera. The image is captured from an oblique angle, while the test article is in the wind tunnel. This allows a qualitative assessment of the uniformity of the heat flux. However, it should be noted that the local heat transfer coefficient would be required to adequately link surface temperature and heat flux.

3.2.2. Calibration and estimation of the distribution of liquid water

A calibration is required for converting the measured capacitance values to a liquid volume fraction. This procedure consists of two steps as described in the following. Subsequently, the method for estimating the distribution of liquid water in the ice layer is explained.

3.2.2.1. Conversion from capacitance to relative permittivity In this study, the dielectric behavior of the ice accretion is modeled as a capacitor and a resistor connected in parallel – as it is common for other moisture measurements in soil and other media [15,5]. In addition, parasitic capacitances due to effects other than the ice accretion – such as the influence of the heater or the wiring – are represented as a capacitor in parallel to the ice layer. The described equivalent circuit of the system is shown in Figure 11.

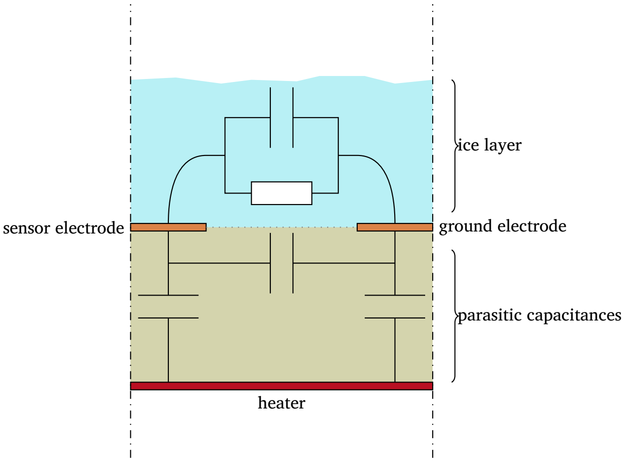

Fig. 11. Equivalent electrical circuit used to model the dielectric properties of the sensor and the ice accretion.

The capacitance of this system can be written as

$$C = C_0 + C_g \overline{\varepsilon_r}, \tag{8}$$

where C_0 includes the parasitic capacitances and C_g is a factor that only depends on the geometry of the electrodes, called the geometric capacitance. $\overline{\varepsilon_r}$ represents an effective relative permittivity of the medium in front of the sensor, weighted according to its sensitivity profile. With the weighting function w due to the sensitivity profile this can be expressed as

$$\overline{\varepsilon_r} = \int_0^\infty w \varepsilon_r \mathrm{d}z. \tag{9}$$

Here ε_r is the local relative permittivity of the ice layer.

Equation (8) contains two parameters, which need to be obtained from a calibration of the sensors. For this purpose the capacitances with two media with known permittivities are measured. The first medium is air with a relative permittivity close to unity and the second medium is isopropanol with a relative permittivity of approximately 20 at 20 °C. For this calibration, the thickness of the isopropanol layer must be sufficiently large such that the electric field beyond the layer can be neglected.

These two measurements at known relative permittivities, where $\overline{\varepsilon_r} = \varepsilon_r$, yield the two parameters in Equation (8).

The geometric capacitance of each sensor can be obtained either from the measurements described above or from numerical simulations of the electric field due to the electrodes. Table 2 gives a comparison of the experimentally and numerically obtained geometric capacitances. The simulation and the experiment are in good agreement.

Table 2
Geometric capacitance obtained from the experiments and from simulations.

	geometric capacitance in pF		
	experiment	simulation	relative deviation
large-scale sensor	7.516	7.263	−3.4 %
near-wall sensor	25.245	26.031	+3.1 %

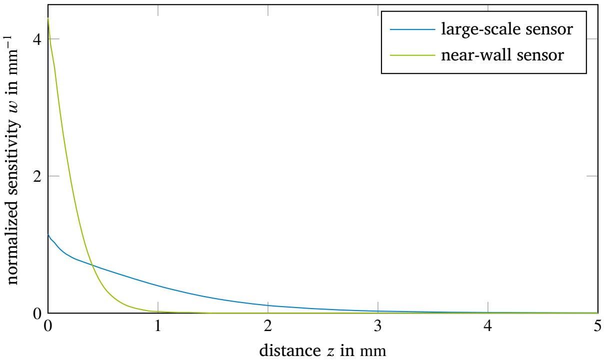

Fig. 12. Sensor sensitivities normalized such that their integrals over the entire domain equals unity.

The simulations enable the calculation of the weighting function w required in Equation (9). For this purpose the simulation has been performed for different ice layer thicknesses up to 20 mm for each sensor. The sensitivity of each sensor can then be obtained as a function of the distance to the sensor plane by taking the derivative of the capacitance with respect to the distance to the sensor. Normalizing the sensitivity such that its integral from zero to infinity equals unity provides the weighting function $w(z)$. The sensitivity at a distance of 20 mm is sufficient to neglect any influence beyond this distance.

The normalized sensitivities are shown in Figure 12 for each sensor.

3.2.2.2. Dielectric properties of wet ice layers The ice accretion is composed of ice, liquid water and air. At the excitation frequencies applied in the present study, the relative permittivity of liquid water of approximately 88 is significantly higher than that of the other two phases. The relative permittivities of ice and air are approximately 3.2 and 1. Due to the value of air being similar to that of ice and due to low volume fraction of air in the ice accretion, the air phase is neglected in the following. Thus, the ice accretion is approximated as a mixture of ice and liquid water.

Several correlations for the effective dielectric properties of mixtures are available. The most widely used correlations are those of Lichtenecker [16], Maxwell Garnett [17] and Bruggeman [18]. In a comparison of multiple correlations to the experimental data of Currie and Fuleki [5], the model of Bruggeman exhibits the best agreement. In this theoretical model the effective relative permittivity $\varepsilon_{\mathrm{r,B}}$ is given implicitly by

$$\varepsilon_{\mathrm{r,B}} = \varepsilon_{\mathrm{r,i}} + \frac{v_{\mathrm{liq}}}{3}(\varepsilon_{\mathrm{r,w}} - \varepsilon_{\mathrm{r,i}}) \sum_{j=x,y,z} \frac{\varepsilon_{\mathrm{r,B}}}{\varepsilon_{\mathrm{r,B}} + g_j(\varepsilon_{\mathrm{r,w}} - \varepsilon_{\mathrm{r,B}})} \tag{10}$$

where $\varepsilon_{\mathrm{r,i}}$ and $\varepsilon_{\mathrm{r,w}}$ denote the relative permittivity of ice and water, respectively. g_x, g_y, g_z are the depolarization factors of the inclusions in the three dimensions in space. For these depolarization factors $g_x + g_y + g_z = 1$ must be valid.

The Bruggeman model assumes that the inclusions are subjected to an effective mean field. However, close to percolation and above the percolation threshold, when the liquid forms large clusters, this assumption is no longer valid [19,20]. At percolation the liquid forms a path through the ice accretion, which results in relative permittivities that are significantly larger than those predicted by effective medium models.

Wiener [21] formulated upper and lower bounds for effective medium approximations. These bounds are given by a laminate parallel to the electric field and a laminate perpendicular to the electric field. However, for a medium which can be considered statistically isotropic on the macroscopic scale, Hashin and Shtrikman [22] proposed narrower bounds. The upper bound is given by liquid water forming a percolation cluster and enclosing spherical inclusions of ice. The upper bound derived by Hashin and Shtrikman is given by

$$\varepsilon_{\mathrm{r,HS}} = \varepsilon_{\mathrm{r,w}} + \frac{1 - v_{\mathrm{liq}}}{(\varepsilon_{\mathrm{r,i}} - \varepsilon_{\mathrm{r,w}})^{-1} + \frac{v_{\mathrm{liq}}}{3\varepsilon_{\mathrm{r,w}}}}. \tag{11}$$

Due to the sudden change in dielectric properties at the percolation threshold, no mixing model is available, which is valid for the full range of liquid volume fractions. Therefore, in the present work, the Bruggeman model is used for liquid volume fractions below percolation and the upper bound proposed by Hashin and Shtrikman is used at higher liquid volume fractions. At intermediate values, the two models are blended.

The relative permittivity of the ice–water mixture is calculated from

$$\varepsilon_{\mathrm{r}} = \frac{1}{2}\left[1 - \tanh\left(\frac{v_{\mathrm{liq}} - v_{\mathrm{liq}}^*}{\gamma}\right)\right]\varepsilon_{\mathrm{r,B}} + \frac{1}{2}\left[1 + \tanh\left(\frac{v_{\mathrm{liq}} - v_{\mathrm{liq}}^*}{\gamma}\right)\right]\varepsilon_{\mathrm{r,HS}}. \tag{12}$$

Here v_{liq}^* describes a threshold for the blending and γ describes half of the width of the blending. These parameters are fitted to the experimental data of Currie and Fuleki. This equation is also in qualitative agreement with measurements of the relative permittivity of wet soil [23,24].

Figure 13 shows the experimental data of Currie and Fuleki [5], the Bruggeman model with the depolarization factors fitted to this data, the equation above and the lower and upper bounds.

3.2.2.3. Estimation of the distribution of liquid water For simplicity, the transport processes in the ice layer are considered as one-dimensional, neglecting any non-uniformity in the ice layer thickness on the sensor. An exemplary three-dimensional scan of an ice layer is presented in subsection 3.3. In this study, the distribution of liquid water v_{liq} in the ice layer is approximated as linear with

$$v_{\mathrm{liq}} \approx v_{\mathrm{liq,0}} + (v_{\mathrm{liq,s}} - v_{\mathrm{liq,0}})\frac{z}{h} \tag{13}$$

with the liquid volume fraction at the substrate $v_{\mathrm{liq,0}}$, the liquid volume fraction at the outer surface of the ice accretion $v_{\mathrm{liq,s}}$, the distance to the wall z and the mean ice thickness h, which is obtained from stereoscopy. This equation contains two unknown parameters $v_{\mathrm{liq,0}}$ and $v_{\mathrm{liq,s}}$, which need to be obtained from measurements. Measurements with the two developed sensors described above, enable the calculation of these parameters, since the sensors have different ranges of sensitivity.

The relative permittivity ε_{r} of the ice accretion is calculated from Equation (12) as described above and evaluated for the liquid water distribution given by Equation (13). The relative permittivity of the air beyond the ice layer is taken to be equal to one, neglecting its ice water content and liquid water content. Thus, the local relative permittivity can be written as

$$\varepsilon_{\mathrm{r}}(v_{\mathrm{liq}}, z) = \begin{cases} \varepsilon_{\mathrm{r}}(v_{\mathrm{liq}}, z) & z \le h \\ 1 & z > h \end{cases} \tag{14}$$

with the average ice accretion thickness h. A further benefit of this method is that it compensates the loss in capacitance, which occurs for cases where the accretion thickness is less than the sensitive range of the sensor.

Given the measurements with the two sensors $\overline{\varepsilon_{\mathrm{r}i}}$, the weighting function w_i plotted in Figure 12 and the relative permittivity obtained

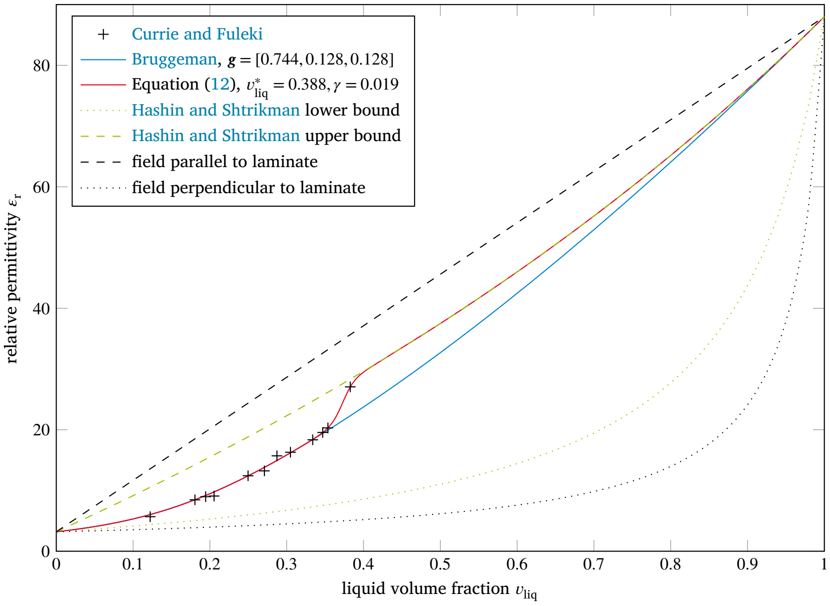

Fig. 13. Comparison of the fitted different dielectric mixing law with the experimental data of Currie and Fuleki. The dashed and the dotted lines correspond to the upper and lower bounds, respectively.

from Equation (14) with Equation (12) for the ice layer permittivity, Equation (9) can be solved numerically to obtain the unknown parameters $v_{\text{liq},0}$ and $v_{\text{liq,s}}$ in the assumed liquid volume fraction distribution given by Equation (13).

These equations give a system of two non-linear equations, which can be solved iteratively. First, the liquid profile is evaluated for an initial guess of the unknown parameters. Based on the obtained liquid profile, the local relative permittivity is calculated. Given this profile of relative permittivity in the ice accretion, the effective relative permittivities that each sensor would measure are calculated. These predicted values are then compared with the actually measured values. The estimate of the parameters $v_{\text{liq},0}$ and $v_{\text{liq,s}}$ is adapted and the procedure repeated.

3.3. Stereoscopy

To convert the liquid mass fraction measured by calorimetry to a volume fraction, the total volume of the ice accretion is required. Furthermore, the ice layer is approximated with a uniform thickness for the capacitive measurement. Therefore, the average thickness of the accretion represents the relevant dimension for these calculations. For this purpose, stereoscopy is utilized to measure the ice layer profile analogous to the work of Connolly et al. [25].

Two synchronized cameras with an angle of approximately 20° between their lines of sight capture the ice accretion process and provide two images from slightly different perspectives. After a calibration of the camera setup, corresponding points in the image pair can be detected and matched using semi-global matching [26]. This procedure yields a so-called disparity map, in which each pixel is assigned a value corresponding to the displacement of the physical point in the two images. Based on the calibration, this shift can be translated to a distance to the camera. From the resulting three-dimensional reconstruction the ice accretion profile is evaluated and integrated to obtain the accreted volume and the mean ice thickness.

Figure 14 shows an exemplary profile of an ice accretion grown on the sensor. While a peak in the profile can be seen at the stagnation point, the accretion can be considered reasonably uniform. The peak is attributed to the effects of erosion. Common models for erosion in the framework of ice crystal icing consider the rate of erosion to be mainly proportional to the square of the tangential velocity component of the impacting ice crystals [3,4,27]. The tangential velocity component vanishes at the stagnation point. Therefore, erosion is expected to have a lesser influence on the accretion thickness at the stagnation point.

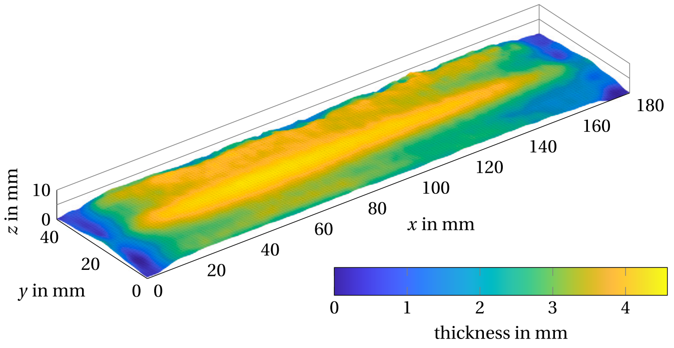

Fig. 14. Exemplary ice accretion profile on the sensor obtained from the stereo vision setup. The mean ice thickness of this scan is 3.4 mm.

4. Results and discussion

In this section, first the results of an exemplary experimental run are presented and discussed in detail. Second, the different influences of wet bulb temperature, heat flux and ice water content on the accretion process are discussed.

The evolution of the ice accretion thickness with the 95 % confidence interval obtained from ten experimental runs is depicted in Figure 15. The graphs show the accretion thickness at the stagnation point averaged over the span of the sensor and measured from shadowgraphy and stereoscopy. The data for stereoscopy is not evaluated in the first 30 s, since the clean test article does not provide sufficient features for the three-dimensional reconstruction. The agreement between shadowgraphy and stereoscopy is typically better than ±0.2 mm. In addition, the mean ice thickness, which is proportional to the accreted volume, obtained from stereoscopy is shown in Figure 15. The process is divided into three stages following the onset of the ice cloud. In the first stage, ice crystals impacting onto the heated substrate cause the formation of drops of meltwater, which coalesce and can build a liquid film on the surface of the test article. This leads to a decreasing surface temperature.

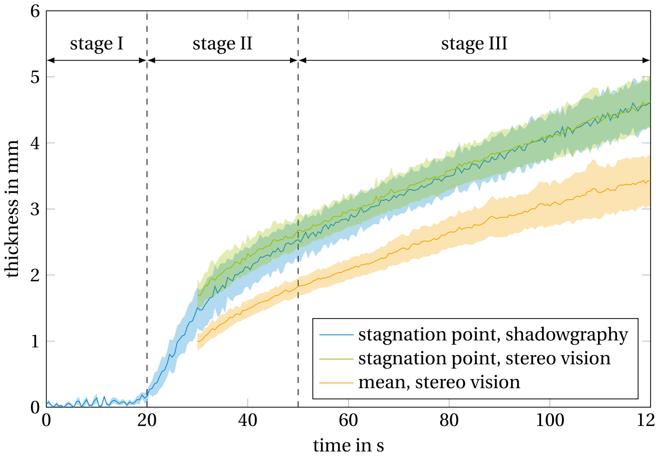

Fig. 15. Evolution of the accretion thickness of an exemplary experimental run. The shaded areas indicate the 95 % confidence intervals obtained from ten experiments. The experimental runs were conducted at a heat flux of 7.2 kW m^{-2}, a wet bulb temperature of −5 °C, a flow velocity of 40 m s^{-1} and an ice water content of 3.9 g m^{-3}.

Figure 16 provides a pictorial illustration of ice accretion initiation and growth on a heated substrate during the course of an exemplary ice crystal accretion run. The inception phase of ice crystal accretion in the Braunschweig icing wind tunnel has been previously investigated and reported by Malik et al. [28].

Figure 17 provides a quantitative overview of evolution of the ice accretion profile, wherein, the lower curve corresponds to a time instant of 20 s after the start of the ice cloud. The time increment between the different curves is 10 s.

The temperature evolution as a result of the impacting ice crystals and the respective heat transfer physics is presented in Figure 18 and has been described in detail by Malik et al. [28]. The temperature sensor is positioned at the corner of the sensor and covered by tape to fix it to the test article. The final temperature therefore remains above the freezing temperature and the obtained values represent only qualitative data.

The protocol of conducting the experiment is such that the surface is first allowed to reach thermal equilibrium and only after that is the icing cloud is switched on, which results in rapid drop of surface temperature, resulting in the transient phase. Moreover, once the surface temperature approaches the freezing temperature, ice starts to accrete on the substrate, which initiates the second stage. Once an ice layer forms on the surface, the surface temperature reaches 0 °C. The focus of the present study is on the stages following ice inception. Therefore, the surface temperature in these stages remains at approximately 0 °C for all parametric combinations. In this second stage, the large amount of meltwater accumulated on the substrate leads to a drastic growth of the ice accretion by promoting crystal adhesion.

Newly adhering ice crystals bind meltwater, splash and thus reduce the liquid fraction at the accretion front. This can be recognized as a sharp decline in liquid volume fraction at the outer surface of the accretion shown in Figure 19. The reduced availability of liquid water at the accretion front results in a decreasing sticking efficiency and thus a decreasing growth rate of the ice layer. In the third stage of the accretion process, the growth rate assumes an approximately constant value, which is in line with an approximately constant liquid volume fraction at the accretion front. On the one hand, liquid water is supplied to the accretion front by water transport through the ice layer driven by the availability of meltwater at the interface to the substrate. On the other hand, adhering ice crystals and convective cooling lead to a decrease in liquid fraction. The constant liquid fraction at the accretion front in the third stage indicates that these water transport effects are in equilibrium. However, it should be noted that the liquid fraction at the interface to the substrate continues to decrease, although it appears to settle at a value of approximately 39 % towards the end of the depicted experimental run.

These results suggest a correlation of sticking efficiency and liquid fraction at the location of impact, which can be evaluated from the gathered data. The sticking efficiency η_s is defined as the mass fraction of impacting ice crystals that remain on the substrate [2]. This can be interpreted as a dimensionless growth rate and is expressed as:

$$\eta_s = \frac{\text{adhering mass flux}}{\text{impacting mass flux}} = \frac{\dot{h}\rho_{acc}}{\eta_c IWC u}, \tag{15}$$

with the growth rate $\dot{h}$, the bulk density of the accretion ρ_{acc}, the collection efficiency η_c, the ice water content IWC and the flow velocity u. In order to minimize the effects of erosion, the growth rate is evaluated at the stagnation point. The density of the accretion is approximated as 940 kg m^{-3}, which accounts for the liquid fraction of the medium. Numerical simulations of particle trajectories impacting on a flat plate test were performed by ONERA within the EU Horizon MUSIC-haic project, which yielded a collection efficiency of $\eta_c = 0.876$. Previously, Malik et al. [28] reported similar values of ice crystal collection efficiencies impacting on a similar flat plate model.

The experimentally obtained correlation between sticking efficiency and liquid fraction at the accretion front in stage II is depicted in Figure 20. This relation is presented for different wet bulb temperatures in the wind tunnel. For each parametric influence, a minimum of four experimental runs were performed to ensure repeatability and confidence in the ice crystal icing experiments, as well as in the measurement techniques.

At a wet bulb temperature of −15 °C, the sticking efficiency appears to increase steeper with increasing liquid fraction than for the other experimental conditions. This could be attributed to the increased sensible heat associated with the particle, which results in a quicker refreezing of the connection between the impacting particle and the ice accretion. However, as this represents an extreme condition, caution should be applied in its interpretation. At low liquid fractions, the data at −2 °C appears to diverge from the other measurements. This is presumably attributed to a lower cooling power provided by the ice crystal cloud. While the wet bulb temperature in the wind tunnel is below freezing, the pipe through which the particles are transported to the wind tunnel is generally around 0 °C. The ice crystals at a wind tunnel temperature of −2 °C are less glaciated compared to cooler temperatures which has some influence on the respective cooling power provided by the icing cloud. This would lead to an increased sticking efficiency which is more pronounced at low liquid fractions at the accretion front, which would otherwise only yield a low sticking efficiency. Nonetheless, the data points at negative wet bulb temperatures agree rather well.

In contrast, the case with a positive wet bulb temperature of +2.5 °C shows a qualitatively different behavior. At this temperature, the particles partially melt in the warm airflow combined with relative flow velocities leading to higher residence time of ice crystals leading to higher melt ratio in the Braunschweig icing wind tunnel compared to other facilities. The sticking efficiency of ice crystals for positive wet bulb temperature cases is quite high at the Braunschweig icing wind tunnel compared to the NRC wind tunnel used by Currie et al. [2] where flow velocities are much higher and ice crystal residence times are shorter also taking into account the length of icing wind tunnels. The partially melted impacting crystals already introduce the liquid water necessary for ice accretion and do not rely on the transport of meltwater through the ice accretion. Thus, the sticking efficiency is determined by the melt ratio and is not a function of the liquid fraction at the impact location. Correspondingly, the growth rate does not decrease significantly, but remains at a constant level. This is illustrated by the evolution of the accretion thickness depicted in Figure 21.

In a parametric study, the influences of wet bulb temperature, substrate heat flux and ice water content in the cloud on liquid volume

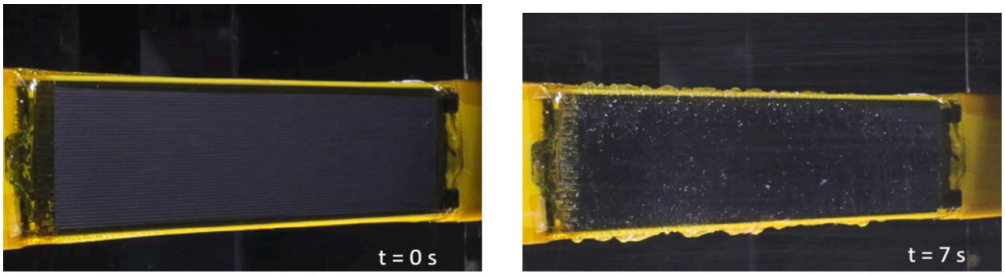

(a) Dry-air configuration – Dry heated substrate (b) Impact of icing cloud – Ice melting (liquid film)

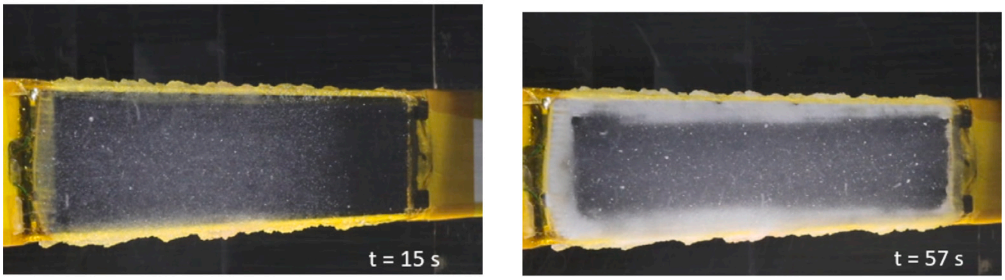

(c) Formation of thin ice layer on heated substrate (d) Growth of ice layer over time

Fig. 16. Snapshots of ice accretion inception and growth over time.

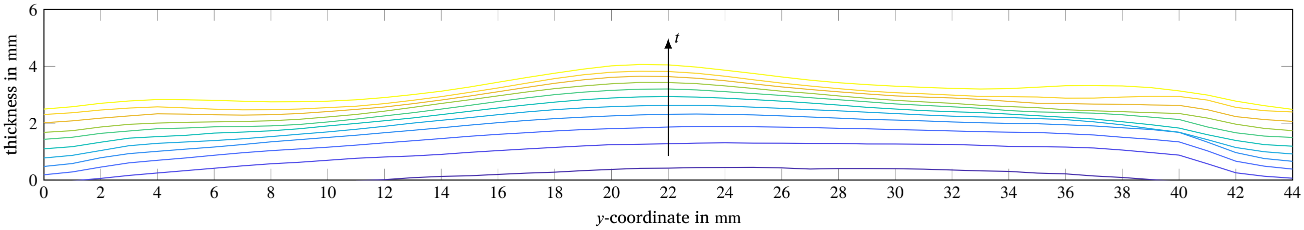

Fig. 17. Evolution of the ice accretion profile. The lower curve corresponds to a time instant 20 s after the start of the ice cloud. The time increment between the different curves is 10 s.

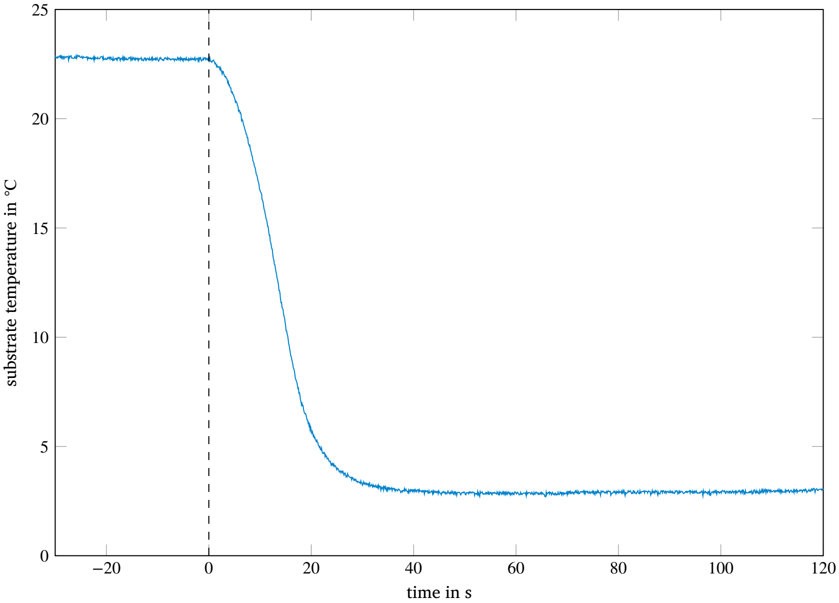

Fig. 18. Qualitative surface temperature evolution as a result of ice crystals impacting onto the heated substrate. The temperature sensor is placed at the corner of the sensor and attached with tape and thus does not completely approach the freezing temperature.

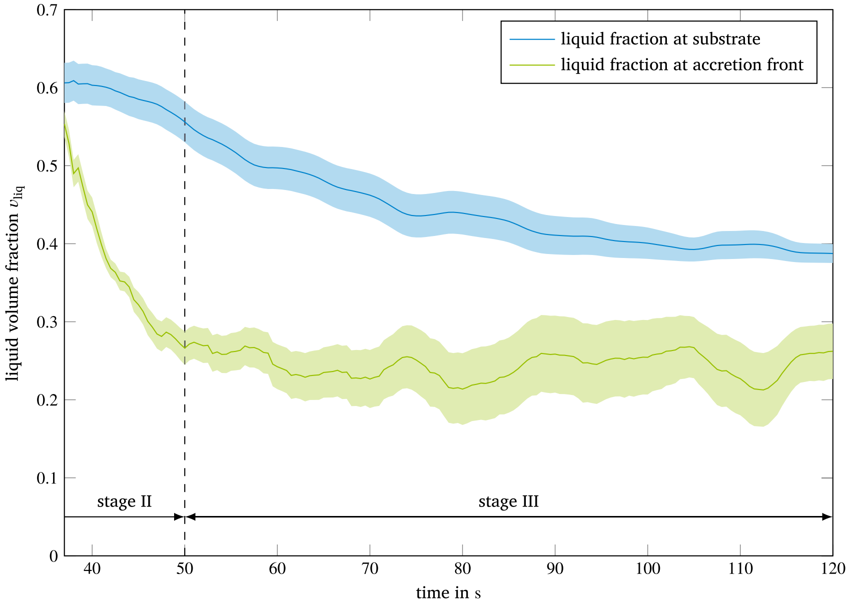

Fig. 19. Distribution of liquid water in the ice accretion as a function of time evaluated from the capacitive measurements.

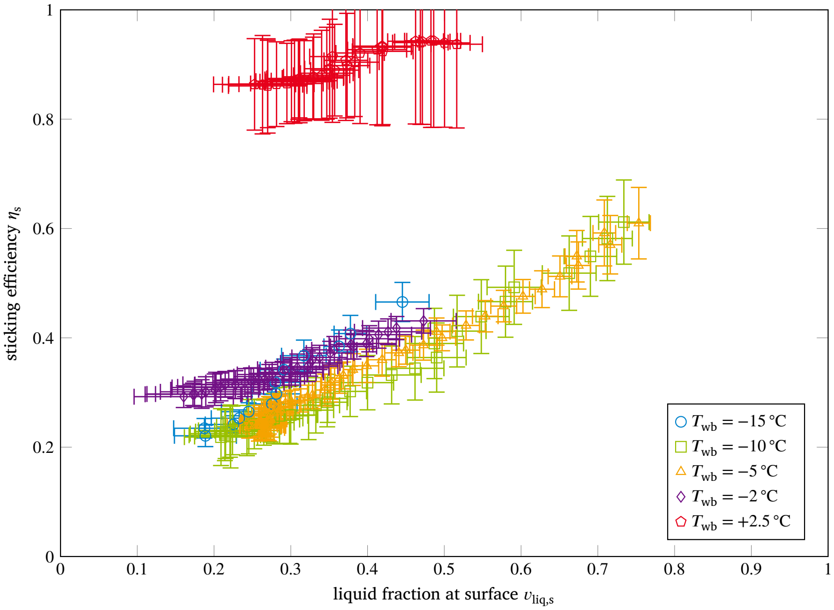

Fig. 20. Experimentally determined relation between sticking efficiency and liquid fraction at the location of impact. The different colors indicate different wet bulb temperatures in the wind tunnel. Despite the negative wet bulb temperature of −2 °C, the particles might be partially melted at this condition.

fraction and sticking efficiency were investigated. The experimental conditions are listed in Table 6 in the appendix.

4.1. Influence of wet bulb temperature

To investigate the influence of wet bulb temperature on the ice accretion process, experiments were carried out in which the wet bulb temperature was varied in a range from −15 °C to +2.5 °C.

For negative wet bulb temperatures, the ice crystals are fully glaciated throughout the transport process until they impact the test article. The necessary condition to initiate ice accretion is dictated by meltwater produced as a result of the heat transfer between the ice crystals and the heated substrate. This meltwater plays a key role in increasing the sticking efficiency of ice crystals in the inception phase. Once the ice layer is formed, the meltwater is imbibed into the ice layer and wets the accretion front and thereby determines the accretion growth process.

At positive wet bulb temperature, melting of ice crystals during transport to the test section leads to the particles being partially melted upon impact. In this case, substrate heating is no longer necessary for ice to accrete.

Unlike the drastic ice accretion growth rates in the case of positive wet bulb temperature, growth rates are much lower at negative wet bulb temperature conditions. The interfacial meltwater generated at the heated substrate first needs to flow through the porous ice layer to reach the outermost surface of the accretion to allow the incoming ice crystals to stick and contribute to the accretion process. Therefore, the imbibition process limits the ice accretion.

The influence of wet bulb temperature on the liquid volume fraction in the ice accretion is shown in Figure 22. The difference in magnitudes

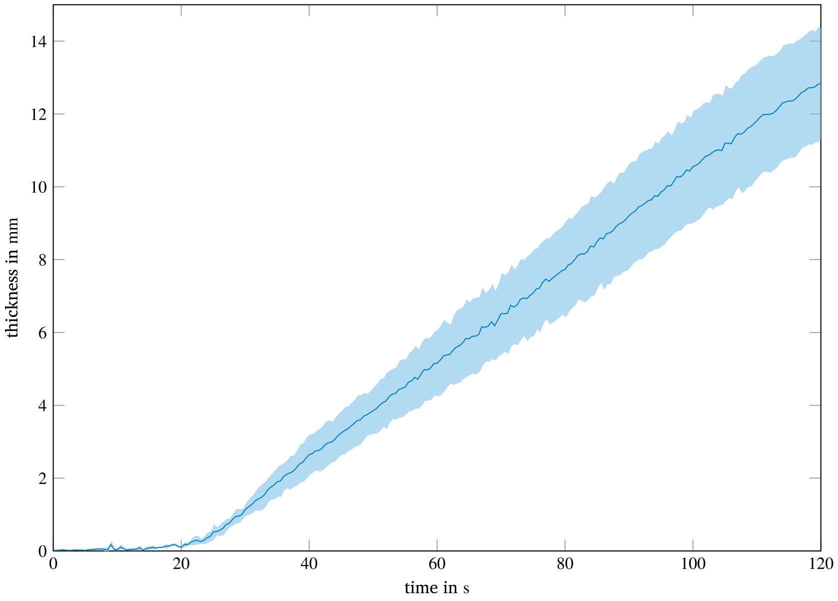

Fig. 21. Ice accretion thickness at the stagnation point as a function of time at a positive wet bulb temperature. The experimental runs were conducted at a heat flux of 7.2 kW m^{-2}, an air temperature of 2.5 °C, a flow velocity of 40 m s^{-1} and an ice water content of 4.0 g m^{-3}.

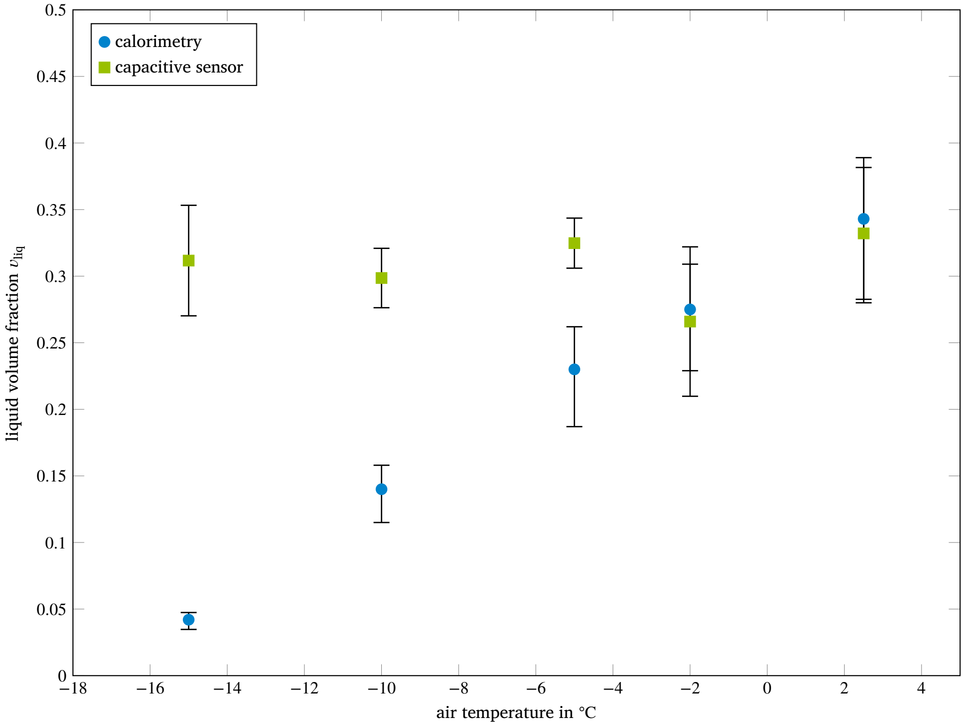

Fig. 22. Influence of wet bulb temperature on liquid volume fraction. The experimental runs were conducted at a heat flux of 7.13 kW m^{-2}, a flow velocity of 40 m s^{-1} and an ice water content of 4.0 g m^{-3}. The air temperature was varied from −15 °C to + 2.5 °C.

between calorimetry and capacitive sensor for low wet bulb temperatures stem from the fact that in the case of calorimetry, the ice layer had to be manually removed and added to the dewar. Since this was done once the run was completed, this meant the very low tunnel temperatures resulted in refreezing of the liquid water in the ice layer inside the tunnel leading to rather low values obtained by calorimetry and should therefore be treated with caution. However, at wet bulb temperatures close to the freezing temperature, the values measured by calorimetry and capacitive measurement agree well.

The influence of wet bulb temperature on the approximately constant sticking efficiency in the third stage of the accretion process is shown in Figure 23. Although the increase in sticking efficiency with increasing wet bulb temperature is gradual for negative wet bulb temperatures and the interpretation is limited by the uncertainty, there is a sudden and sharp rise for the case with positive wet bulb temperature. This is again attributed to melt ratio, which dominates the growth process leading to high sticking efficiencies that are not limited by water transport through the ice layer.

A similar trend is observed for the final ice layer thickness at the stagnation point shown in Figure 24. An increasing wet bulb temperature results in an increase in ice accretion thickness. It should be noted that this is the result of all three stages of ice accretion. An extended

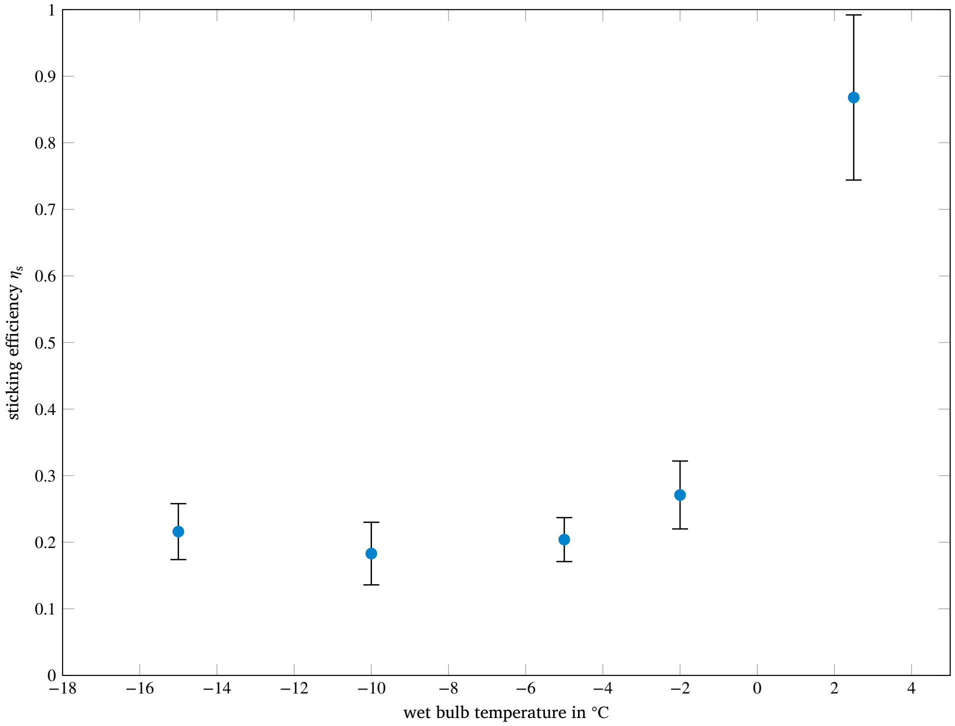

Fig. 23. Influence of wet bulb temperature on sticking efficiency in stage III. The experimental runs were conducted at a heat flux of $7.13\,\mathrm{kW\,m^{-2}}$, a flow velocity of $40\,\mathrm{m\,s^{-1}}$ and an ice water content of $4.0\,\mathrm{g\,m^{-3}}$. The air temperature was varied from −15 °C to +2.5 °C.

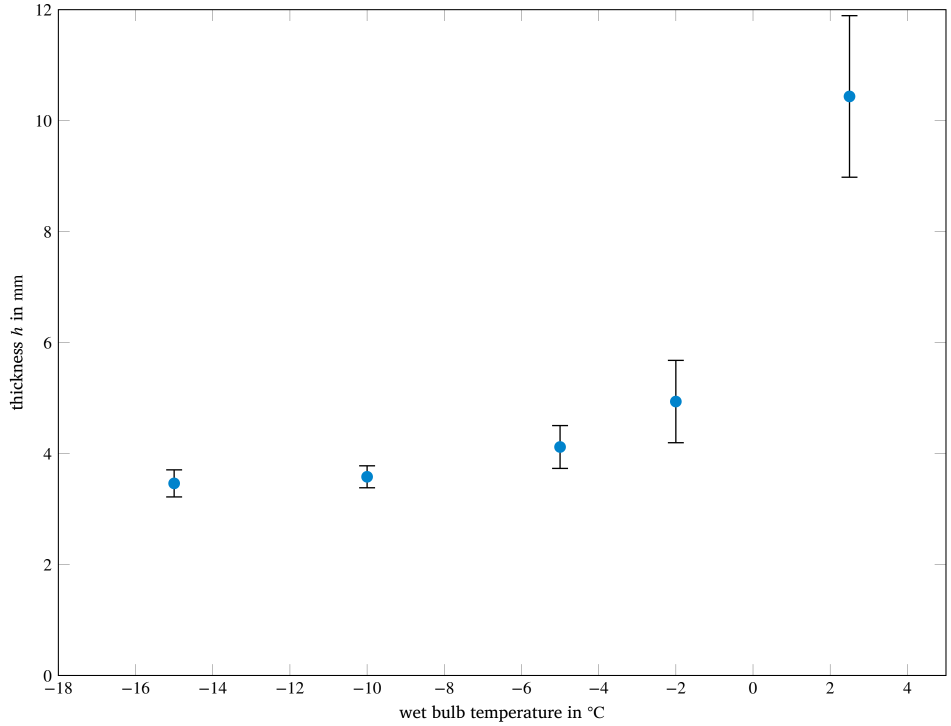

Fig. 24. Influence of wet bulb temperature on the average thickness 80 s after ice inception. The experimental runs were conducted at a heat flux of $7.13\,\mathrm{kW\,m^{-2}}$, a flow velocity of $40\,\mathrm{m\,s^{-1}}$ and an ice water content of $4.0\,\mathrm{g\,m^{-3}}$. The air temperature was varied from −15 °C to +2.5 °C.

first stage results in more accumulated meltwater at the beginning of the second stage, which results in a more drastic growth.

The porosity of the ice layer and the saturation of the pores calculated from the calorimetry data are specified in Table 3. It appears that the saturation increases with increasing wet bulb temperature. However, this trend is affected by the potential refreezing of meltwater after the end of the experimental run. Due to the minor accreted volume at the lowest investigated wet bulb temperature, the relative error in the measured volume can be expected to be large. Therefore, the large porosity measured at this condition should be interpreted with caution. However, for the other cases, the porosity appears to scatter in the range of 25 % to 37 %.

Table 3
Porosity and saturation calculated for different wet bulb temperature conditions. Due to refreezing of liquid water in the ice layer at very low temperature, the porosity and saturation results for Case 6 marked with * should be treated with caution.

Case	T_{wb} in °C	Porosity	Saturation
6*	-15	0.61	0.07
7	-10	0.33	0.52
8	-5	0.25	0.95
9	-2	0.37	0.72
10	+2.5	0.35	0.98

4.2. Influence of substrate heat flux

To investigate the influence of the average heat flux at the substrate on the ice accretion process, the heating power is supplied by the heating film is varied in a parametric study. The average heat flux ranges from $4.5\,\mathrm{kW\,m^{-2}}$ to $12.8\,\mathrm{kW\,m^{-2}}$.

A change in heat flux has a variety of consequences. The steady state substrate temperature prior to the start of the ice cloud increases with increasing heat flux. This leads to a prolonged first stage of ice accretion, since the onset of accretion is delayed due to the larger heat stored in the substrate. Consequently, at the beginning of the second stage, more meltwater is accumulated on the substrate, which results in a more severe and extended ice layer growth. Furthermore, when the ice layer develops, a larger heat flux results in an increased supply of meltwater at the interface to the substrate. On the one hand, this can lead to shedding of the accretion. This has been shown by Kintea et al. [6], who modeled shedding by defining a critical threshold for the melted fraction at the interface to the substrate. On the other hand, an increased supply of meltwater contributes to an increased growth rate, since more water is transported through the ice accretion to the accretion front. However, it is observed in the experiments that at a high heat flux, more runback ice forms at the edges of the test article. This suggests that not all liquid water is transported through the ice accretion, but a fraction of it flows along the surface of the substrate and freezes when exposed to the cold airflow.

As can be seen in Figure 25, for the range of tested conditions, with increasing substrate heat flux, the average liquid volume fraction increases for the measurements obtained by calorimetry. However, for the capacitive measurements, the liquid fraction seems to decrease, while the uncertainty increases. This counter-intuitive trend is presumably caused by the thicker ice layers and a nonlinear liquid profile in the accretion, which violate the linear assumptions made for evaluating the capacitive data. The increased volume of runback ice, resulting from liquid flowing along the substrate to the edges of the test article, indicate a more complex liquid profile that deviates from the linear assumption.

The sticking efficiency in the third stage shown in Figure 26 suggests an increasing trend in sticking efficiency with increasing heat flux. However, the large scatter in the experiments results in a notable uncertainty, which limits the interpretation of the data. On the one hand, the rate at which meltwater is generated at the interface to the substrate increases with increasing heating power. This results in more liquid water flowing through the ice layer, which enhances the sticking efficiency. On the other hand, meltwater flowing along the surface of the substrate, leading to runback ice, does not increase the thickness of the ice layer and thus does not yield and increase in sticking efficiency.

This is also reflected in the trends for ice accretion thickness with increasing heat flux, which is shown in Figure 27. The additional formation of runback ice at high heat fluxes dampens the increase in accretion thickness at high heat fluxes.

The formation of runback ice, caused by meltwater escaping the ice accretion, is likely caused by a increased saturation, which is indicated in the data presented in Table 4. The increased amount of runback ice results in considerable ice accretion along the top and bottom edges of the test article. This additional accreted ice is not accounted for in the ice layer volume calculation. From the qualitative observation of accreted ice at the end of these high heat flux cases, it is estimated that this additional ice contributes to an underprediction of around 15 % in accreted volume. This affects the respective porosity and saturation values for those test cases with corrected values documented as +15 % in Table 4.

4.3. Influence of ice water content

To study the influence of ice water content (IWC) on the accretion process, this quantity is varied in the range from $3.7\,\mathrm{g\,m^{-3}}$ to $7.6\,\mathrm{g\,m^{-3}}$. The IWC determines the mass of ice crystals per volume of the flow. Therefore, higher IWC leads to more ice crystals impinging on the surface resulting in an accelerated accretion process.

The accretion growth process results from two competing influences: heating from the substrate and cooling from the icing cloud. In other words, the ice–water composition of the ice layer is the driving force for this process. On the one hand, increasing heat flux generates more interfacial meltwater. On the other hand, for a heated substrate, increasing IWC changes the composition of the ice-water layer from purely liquid water to a semi-frozen (i.e., mixed phase) layer, which is more conducive to ice accretion, until it reaches a threshold beyond which a further increase in IWC leads to more pronounced erosion effects.

The liquid fraction of ice accretions grown at different IWC is shown in Figure 28. Both calorimetry and capacitive measurement show no effect of IWC on the composition of the ice accretion.

It is interesting to note that upon increasing the ice water content, the sticking efficiency drops especially for high ice water content, as can be recognized in Figure 29. This can be explained by effects of erosion, which are not accounted for in the calculation of the sticking efficiency. The large mass flux of ice crystals impacting the ice layer appears to result in more eroded ice, which is also apparent in the shape of the ice accretion, where the peak at the stagnation point is more pronounced. As highlighted earlier, the sticking efficiency describes the ratio of the adhering mass flux to the impacting mass flux. An increased IWC results in an increased absolute impacting mass flux, which, at an approximately constant sticking efficiency, results in an increased adhering mass flux. This yields an increased ice layer thickness, as can be seen in Figure 30.

The effect of IWC on the final accretion thickness can be recognized in Figure 30. The accretion thickness increases with increasing IWC, since more ice crystals are impacting onto the ice layer. The porosity and saturation of the ice accretions are listed in Table 5. The experiments at higher IWC appear to have a lower saturation. A clear trend for this influence can be established by performing further experiments for different substrate heat fluxes and higher IWCs to further consolidate the findings for the said influence.

5. Conclusions

In this study, a quantitative analysis of the ice accretion process is presented with particular focus on quantification of volumetric liquid water content in the ice layer, sticking efficiency and ice thicknesses for a wide range of experimental conditions. To measure the liquid fraction, the two techniques of calorimetry and capacitive measurement are utilized and cross-compared. The experiments are carried out in the Braunschweig icing wind tunnel, capable of simulating ice crystal icing conditions with crystal morphology similar to those found in natural convective conditions.

An optical setup consisting of multiple cameras and light sources is employed to quantify the evolution of maximum thickness and volume of the accreted ice layers, which enabled the calorimetry technique to quantify the volumetric liquid water content. In addition to calorimetry, two capacitive sensors are specially designed to quantify the liquid water content in the near-wall region and on a larger scale. These capacitive sensors enable quantifying the distribution of liquid water in

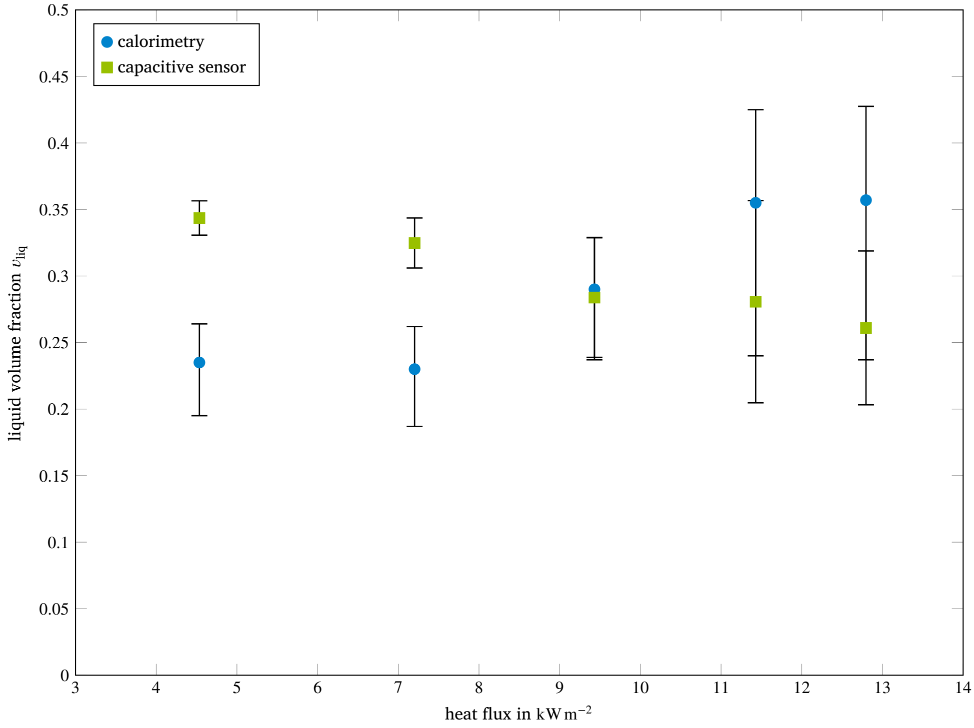

Fig. 25. Influence of substrate heat flux on liquid volume fraction. The experimental runs were conducted at a wet bulb temperature of −5 °C, a flow velocity of 40 m s^{-1} and an ice water content of 4.0 g m^{-3}. The substrate heat flux was varied from 4.54 kW m^{-2} to 12.80 kW m^{-2}.

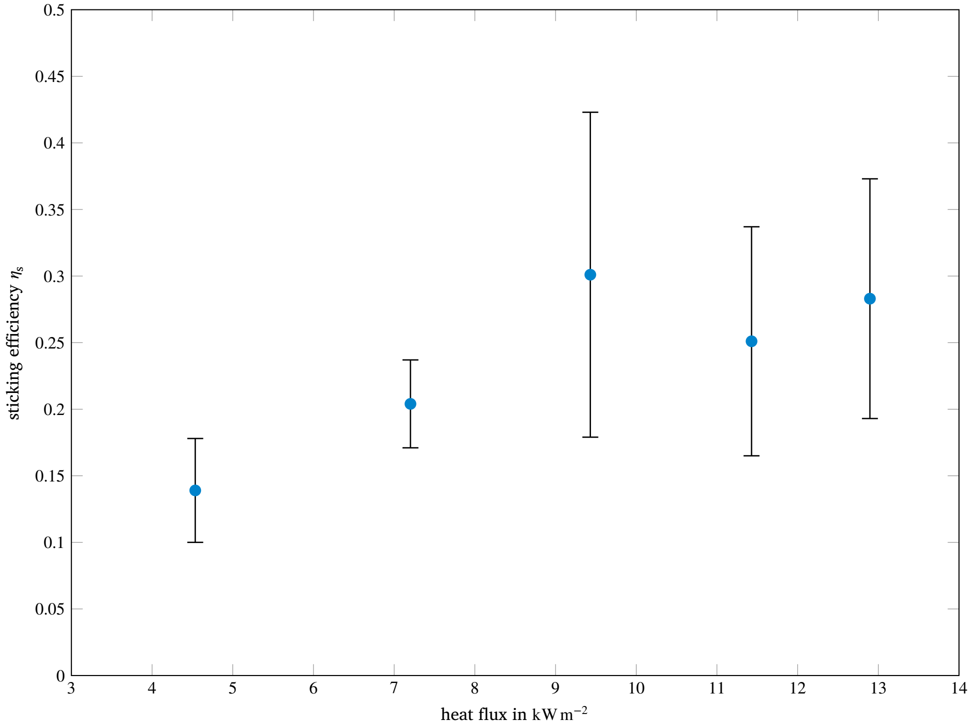

Fig. 26. Influence of substrate heat flux on sticking efficiency in stage III. The experimental runs were conducted at a wet bulb temperature of −5 °C, a flow velocity of 40 m s^{-1} and an ice water content of 4.0 g m^{-3}. The substrate heat flux was varied from 4.54 kW m^{-2} to 12.80 kW m^{-2}.

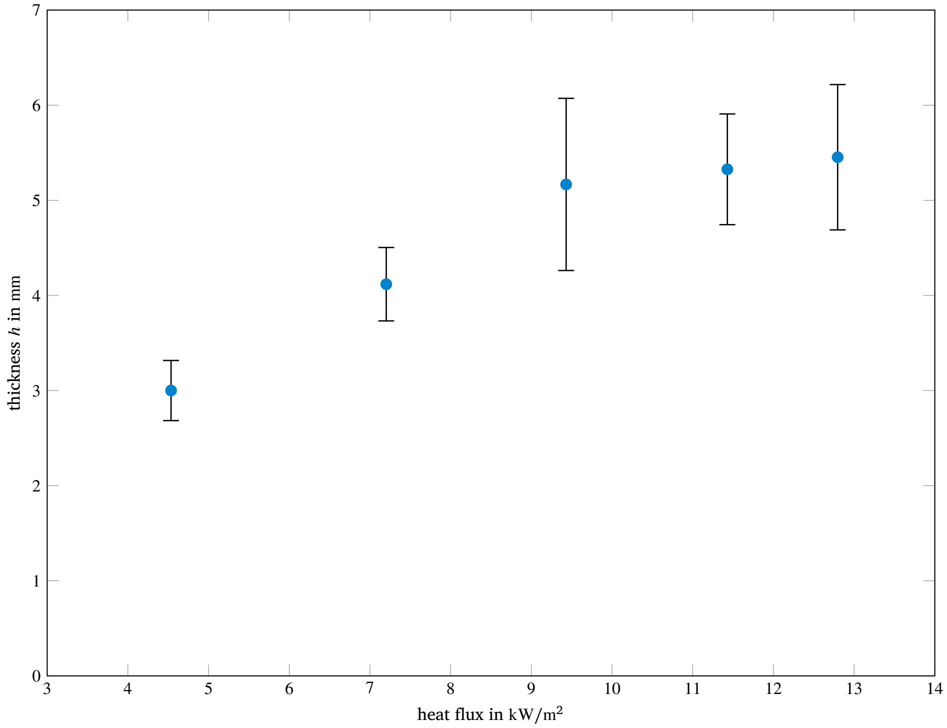

Fig. 27. Influence of substrate heat flux on the ice thickness 80 s after ice inception. The experimental runs were conducted at a wet bulb temperature of −5 °C, a flow velocity of 40 m s^{-1} and an ice water content of 4.0 g m^{-3}. The substrate heat flux was varied from 4.54 kW m^{-2} to 12.80 kW m^{-2}.

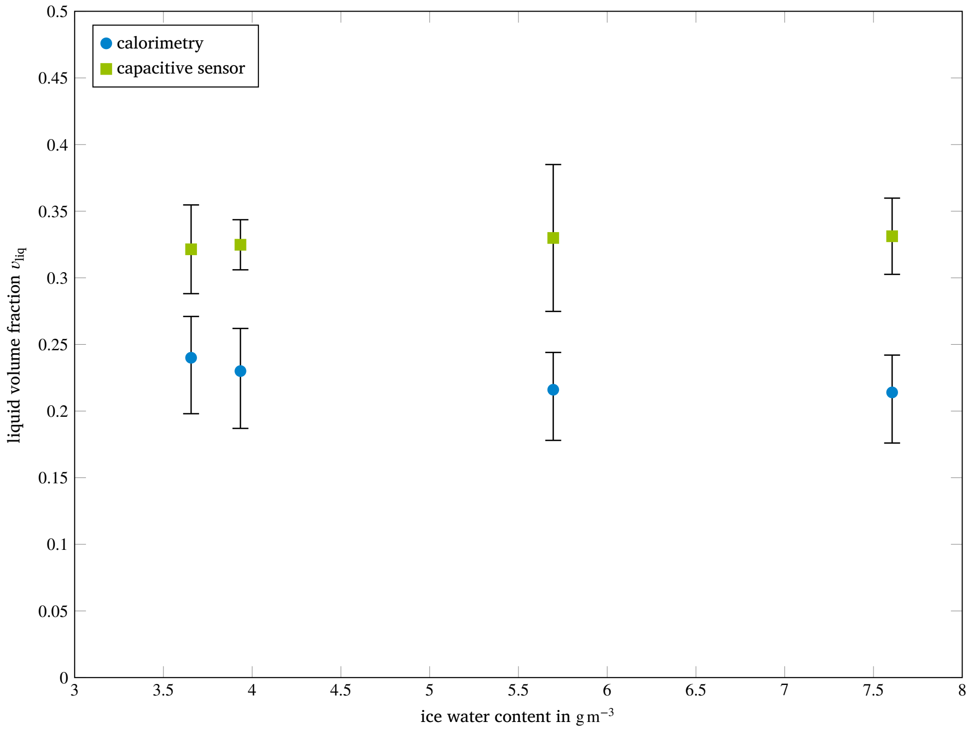

Fig. 28. Liquid volume fraction as a function of ice water content. The experimental runs were conducted at a wet bulb temperature of −5 °C, substrate heat flux of 7.13 kW m^{-2} and a flow velocity of 40 m s^{-1}. The ice water content was varied from 3.6 g m^{-3} to 8 g m^{-3}.

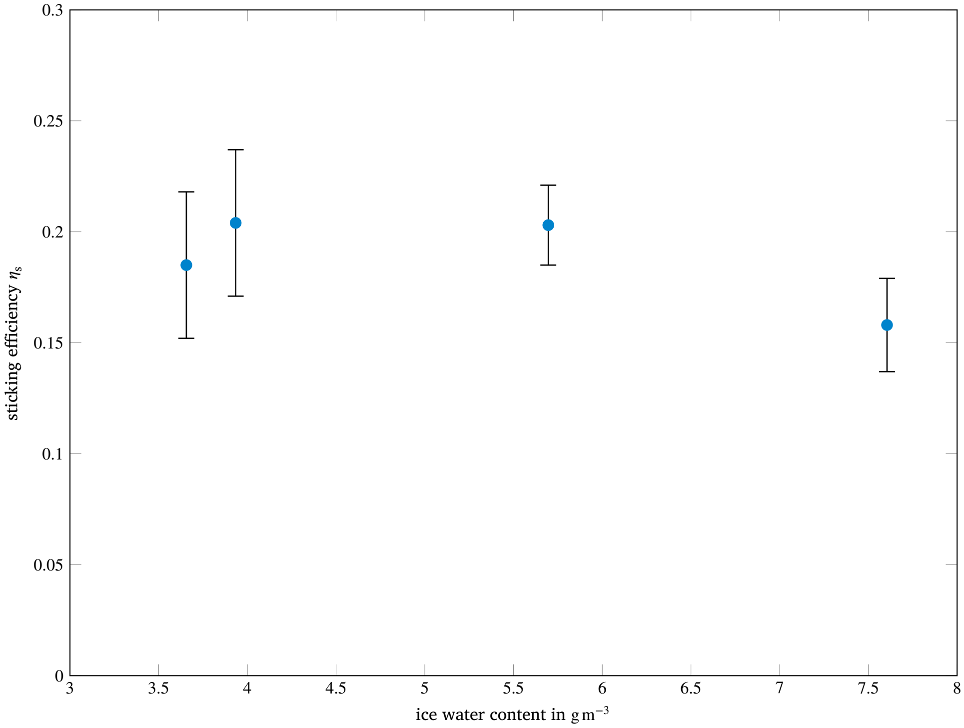

Fig. 29. Influence of ice water content on sticking efficiency in stage III. The experimental runs were conducted at a wet bulb temperature of −5 °C, substrate heat flux of 7.13 kW m^{-2} and a flow velocity of 40 m s^{-1}. The ice water content was varied from 3.6 g m^{-3} to 8 g m^{-3}.

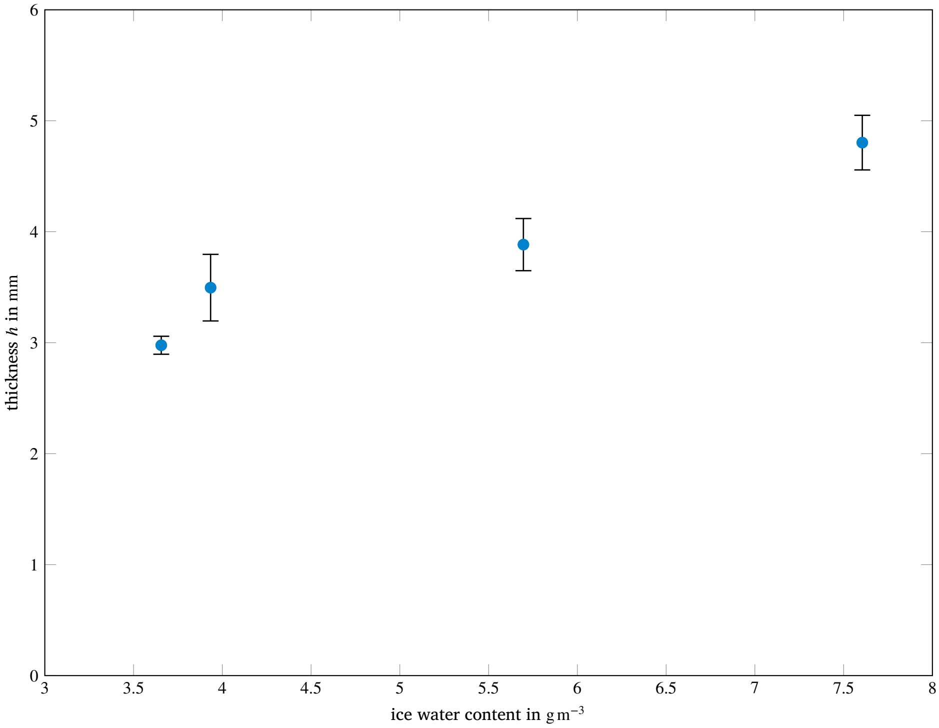

Fig. 30. Influence of IWC on average thickness 60 s after ice inception. The experimental runs were conducted at a wet bulb temperature of −5 °C, substrate heat flux of 7.13 kW m^{-2} and a flow velocity of 40 m s^{-1}. The ice water content was varied from 3.6 g m^{-3} to 8 g m^{-3}.

Table 4
Porosity and saturation calculated for ice accretions formed at different substrate heat fluxes. The columns indicated with +15 % account for an estimation of the runback ice formed on the sides of the test article.

Case	Heat flux in $\mathrm{kW\,m^{-2}}$	Substrate temperature in °C	Porosity	Porosity (+15 %)	Saturation	Saturation (+15 %)
1	4.5	14	0.24	–	0.91	–
2	7.2	23	0.25	–	0.95	–
3	9.4	32	0.28	–	1.0	–
4	11.4	39	0.15	0.32	1.82	0.90
5	12.8	46	0.18	0.35	1.90	0.81

Table 5
Porosity and saturation of ice layers grown at different ice water contents.

Case	IWC in $\mathrm{g\,m^{-3}}$	Porosity	Saturation
11	3.45	0.27	0.87
12	3.96	0.25	0.95
14	5.85	0.37	0.58
13	7.41	0.35	0.60

the accretion layer. This enables the estimation of the mean liquid water content in the ice layer which is used to compare the results with the calorimetry technique.

The accretion process is divided into three stages. In the initial stage, the substrate cools down and meltwater accumulates on its surface. The second stage of ice accretion starting with the onset of accretion is determined by meltwater accumulated on the substrate from the previous stage. This excess liquid water results in a high growth rate. In the subsequent third stage, the supply of liquid water to the accretion front and the reduction of liquid fraction at the surface due to newly adhering ice crystals are in equilibrium and result in a constant liquid fraction at the accretion front and a constant growth rate.

On one hand, the capacitive measurement reveals the correlation between sticking efficiency and liquid volume fraction at the accretion front, which was previously not available from experimental investigations. On the other hand, the calorimetry measurement technique provides means to determine the mass fraction, volumetric liquid fraction, porosity and saturation of slushy and glaciated ice layers. The experiments highlight the increasing trend in sticking efficiency with increasing liquid fraction at the location of impact.

For an increasing wet bulb temperature, the sticking efficiency and maximum thickness of ice layer increase. This increase is especially pronounced when switching to positive wet bulb temperatures. While at negative wet bulb temperatures, the accretion is limited by the water transport through the ice layer, the particles are partially melted at positive wet bulb temperatures, which yields a more severe ice accretion. For an increasing heat flux from the substrate, a similar trend is observed for sticking efficiency and maximum thickness of the ice layers accreted on the surface. This is attributed to an increased generation of meltwater at the interface to the substrate, wetting the accretion front and resulting in an increase in sticking efficiency and accretion thickness. Moreover, the influence of ice water content was also investigated and it was found that for the tested conditions, upon increasing the ice water content whilst the maximum thickness increased, the sticking efficiency dropped for high ice water contents. This is presumably attributed to more pronounced effects of erosion, which are not accounted for in the calculation of the sticking efficiency.

The main limitation of using calorimetry to obtain the liquid fraction is the swift removal of ice layers from the test articles as soon as the heaters are turned off and thus at very low wet bulb temperatures avoiding refreezing of liquid water to ice. To overcome this limitation, instead of manually removing the ice with an ice scraper, future studies can focus on devising a more sophisticated mechanism of swift ice removal from the substrate without compromising the structural integrity of the test article. This will further enhance the confidence in the measurement technique at very low wet bulb temperatures. On the other hand, with regards to capacitive sensing, the assumption of a linear profile inside the ice layer is the most critical point. Having more than the two sensors would allow for more sophisticated equations to model the liquid distribution, which can be investigated in detail as part of a future study to further enhance the accuracy of the presented results.

To summarize, the presented study provides a comprehensive experimental dataset for more accurate modeling of sticking efficiency in the ice accretion process. The findings of this study are inline with earlier investigations of ice crystal icing on heated and non-heated substrates and provides additional value towards better understanding of ice crystal icing physics on heated substrates.

CRediT authorship contribution statement

Yasir A. Malik: Conceptualization, Data curation, Formal analysis, Investigation, Methodology, Resources, Software, Validation, Visualization, Writing – original draft, Writing – review & editing. **Kilian Köbschall:** Conceptualization, Data curation, Formal analysis, Investigation, Methodology, Resources, Software, Validation, Visualization, Writing – original draft, Writing – review & editing. **Stephan Bansmer:** Conceptualization, Funding acquisition, Supervision. **Cameron Tropea:** Funding acquisition, Methodology, Supervision. **Jeanette Hussong:** Methodology, Supervision. **Philippe Villedieu:** Conceptualization, Funding acquisition, Methodology, Project administration, Writing – review & editing.

Declaration of competing interest

The authors declare the following financial interests/personal relationships which may be considered as potential competing interests:

Kilian Koebschall reports financial support was provided by European Commission. Yasir A. Malik reports financial support was provided by European Commission. Philippe Villedieu reports financial support was provided by European Commission.

Data availability

Data will be made available on request.

Acknowledgements

This project has received funding from the European Union's Horizon 2020 research and innovation programme under grant agreement No 767560.

The authors would like to acknowledge the contribution of Christoph Henniges and Ashuthosh Shridhar for their assistance in carrying out the experimental campaign.

Appendix

Table 6
Experimental conditions of the wind tunnel experiments. Each experiment has been repeated at least three times.

Case	Airspeed in $\mathrm{m\,s^{-1}}$	Wet bulb temperature in °C	IWC in $\mathrm{g\,m^{-3}}$	Heat flux in $\mathrm{kW\,m^{-2}}$
1	40	-5	3.99	4.54
2	40	-5	3.93	7.19
3	40	-5	3.89	9.41
4	40	-5	3.54	11.43
5	40	-5	3.37	12.80
6	40	-15	4.06	7.13
7	40	-10	3.73	7.13
9	40	-2	3.94	7.13
10	40	+2.5	4.04	7.13
11	40	-5	3.66	7.13
13	40	-5	7.61	7.13
14	40	-5	5.70	7.13

References

[1] J. Mason, W. Strapp, P. Chow, The ice particle threat to engines in flight, in: 44th AIAA Aerospace Sciences Meeting and Exhibit, 2006, p. 206.

[2] T.C. Currie, D. Fuleki, A. Mahallati, Experimental studies of mixed-phase sticking efficiency for ice crystal accretion in jet engines, in: 6th AIAA Atmospheric and Space Environments Conference, 2014, p. 3049.

[3] A. Baumert, S. Bansmer, P. Trontin, P. Villedieu, Experimental and numerical investigations on aircraft icing at mixed phase conditions, Int. J. Heat Mass Transf. 123 (2018) 957–978, https://doi.org/10.1016/j.ijheatmasstransfer.2018.02.008.

[4] P. Trontin, P. Villedieu, A comprehensive accretion model for glaciated icing conditions, Int. J. Multiph. Flow 108 (2018) 105–123, https://doi.org/10.1016/j.ijmultiphaseflow.2018.06.023.

[5] T. Currie, D. Fuleki, Development and application of an impedance-based instrument for measuring the liquid fraction and thickness of ice crystal accretions, in: SAE 2015 International Conference on Icing of Aircraft, Engines, and Structures, SAE Technical Paper Series, SAE International, 2015, https://doi.org/10.4271/2015-01-2134.

[6] D. Kintea, I. Roisman, C. Tropea, Transport processes in a wet granular ice layer: model for ice accretion and shedding, Int. J. Heat Mass Transf. 97 (2016) 461–472.

[7] Z. Fournier, D. Geromichalos, S. Herminghaus, M.M. Kohonen, F. Mugele, M. Scheel, M. Schulz, B. Schulz, C. Schier, R. Seemann, A. Skudelny, Mechanical properties of wet granular materials, J. Phys. Condens. Matter 17 (2005) S477–S502, https://doi.org/10.1088/0953-8984/17/9/013.

[8] S.E. Bansmer, A. Baumert, S. Sattler, I. Knop, D. Leroy, A. Schwarzenboeck, T. Jurkat-Witschas, C. Voigt, H. Pervier, B. Esposito, Design, construction and commissioning of the Braunschweig icing wind tunnel, Atmos. Meas. Tech. 11 (2018) 3221–3249.

[9] A. Baumert, Experimental and Numerical Studies on Ice Crystal Icing of Civil Aircraft, TU Braunschweig-Niedersächsisches Forschungszentrum für Luftfahrt, 2019.

[10] M. Breiling, M. Bacher, S. Sokratov, F.G. Best, Method and device for producing snow, 2016, US Patent 9,429,348.

[11] C. Voigt, U. Schumann, P. Jessberger, T. Jurkat, A. Petzold, J.-F. Gayet, M. Krämer, T. Thornberry, D. Fahey, Extinction and optical depth of contrails, Geophys. Res. Lett. 38 (2011).

[12] A. Baumert, S. Bansmer, S. Sattler, H. Pervier, B. Esposito, Simulating natural ice crystal cloud conditions for icing wind tunnel experiments-a review on the design, commissioning and calibration of the tu Braunschweig ice crystal generation system, in: 8th AIAA Atmospheric and Space Environments Conference, 2016, p. 4053.

[13] T. Hauk, E. Bonaccurso, P. Villedieu, P. Trontin, Theoretical and experimental investigation of the melting process of ice particles, J. Thermophys. Heat Transf. 30 (2016) 946–954.

[14] B.L. Dunicz, Water equivalent of vacuum flask calorimeter by the ice fusion method, J. Chem. Educ. 37 (1960) 635.

[15] M. Bittelli, M. Flury, K. Roth, Use of dielectric spectroscopy to estimate ice content in frozen porous media, Water Resour. Res. 40 (2004), https://doi.org/10.1029/2003WR002343.

[16] K. Lichtenecker, Die Dielektrizitätskonstante natürlicher und künstlicher Mischkörper, Z. Phys. 27 (1926) 115–133.

[17] J.C. Maxwell Garnett, Colours in metal glasses and in metallic films, Philos. Trans. R. Soc. Lond., Ser. A, Contain. Pap. Math. Phys. Character 203 (1904) 385–420, https://doi.org/10.1098/rsta.1904.0024.

[18] D.A.G. Bruggeman, Berechnung verschiedener physikalischer Konstanten von heterogenen Substanzen. I. Dielektrizitätskonstanten und Leitfähigkeiten der Mischkörper aus isotropen Substanzen, Ann. Phys. 416 (1935) 636–664, https://doi.org/10.1002/andp.19354160705.

[19] R. Zallen (Ed.), The Physics of Amorphous Solids, Wiley-VCH Verlag GmbH, Weinheim, Germany, 1998.

[20] S. Kirkpatrick, Percolation and conduction, Rev. Mod. Phys. 45 (1973) 574–588, https://doi.org/10.1103/RevModPhys.45.574.

[21] O. Wiener, Zur Theorie der Refractionskonstanten, in: Berichte über die Verhandlungen der Königlich-Sächsischen, in: Mathematisch-Physikalische Klasse, vol. 62, Gesellschaft der Wissenschaften zu Leipzig, 1910, pp. 256–277.

[22] Z. Hashin, S. Shtrikman, A variational approach to the theory of the effective magnetic permeability of multiphase materials, J. Appl. Phys. 33 (1962) 3125–3131, https://doi.org/10.1063/1.1728579.

[23] J. Liu, S. Zhao, L. Jiang, L. Chai, F. Wu, The influence of organic matter on soil dielectric constant at microwave frequencies (0.5–40 GHz), in: 2013 IEEE International Geoscience and Remote Sensing Symposium - IGARSS, IEEE, 2013, pp. 13–16.

[24] T.J. Kelleners, D.A. Robinson, P.J. Shouse, J.E. Ayars, T.H. Skaggs, Frequency dependence of the complex permittivity and its impact on dielectric sensor calibration in soils, Soil Sci. Soc. Am. J. 69 (2005) 67–76, https://doi.org/10.2136/sssaj2005.0067a.

[25] J. Connolly, M. McGilvray, D.R. Gillespie, Optical measurement of ice crystal icing on a NACA 0018 airfoil, in: AIAA AVIATION 2022 Forum, American Institute of Aeronautics and Astronautics, Reston, Virginia, 2022, https://doi.org/10.2514/6.2022-3699.

[26] H. Hirschmuller, Accurate and efficient stereo processing by semi-global matching and mutual information, in: 2005 IEEE Computer Society Conference on Computer Vision and Pattern Recognition (CVPR'05), IEEE, 2005, pp. 807–814, https://doi.org/10.1109/CVPR.2005.56.

[27] Y.A. Malik, L. Bennani, A. Vorgias, P. Trontin, P. Villedieu, Experimental and numerical investigation of ice crystal icing on a heatable NACA0012 airfoil, in: AIAA AVIATION 2022 Forum, 2022, p. 3534.

[28] Y.A. Malik, L. Bennani, S. Bansmer, P. Trontin, P. Villedieu, Experimental and numerical investigation of accretion inception and heat transfer physics in ice crystal icing, Int. J. Heat Mass Transf. 214 (2023) 124364, https://doi.org/10.1016/j.ijheatmasstransfer.2023.124364, https://www.sciencedirect.com/science/article/pii/S0017931023005100.